Lab on a Chip

ROYAL SOCIETY OF CHEMISTRY

PAPER

View Article Online
View Journal | View Issue

Check for updates

Cite this: *Lab Chip*, 2020, **20**, 2889

On-chip analysis of atmospheric ice-nucleating particles in continuous flow†‡

Mark D. Tarn, *[ab] Sebastien N. F. Sikora, [a] Grace C. E. Porter, [ab] Bethany V. Wyld, [a] Matan Alayof,[c] Naama Reicher, [c] Alexander D. Harrison, [a] Yinon Rudich, [c] Jung-uk Shim *[b] and Benjamin J. Murray *[a]

Received 11th March 2020,
Accepted 6th July 2020

DOI: 10.1039/d0lc00251h

rsc.li/loc

Ice-nucleating particles (INPs) are of atmospheric importance because they catalyse the freezing of supercooled cloud droplets, strongly affecting the lifetime and radiative properties of clouds. There is a need to improve our knowledge of the global distribution of INPs, their seasonal cycles and long-term trends, but our capability to make these measurements is limited. Atmospheric INP concentrations are often determined using assays involving arrays of droplets on a cold stage, but such assays are frequently limited by the number of droplets that can be analysed per experiment, often involve manual processing (*e.g.* pipetting of droplets), and can be susceptible to contamination. Here, we present a microfluidic platform, the LOC-NIPI (Lab-on-a-Chip Nucleation by Immersed Particle Instrument), for the generation of water-in-oil droplets and their freezing in continuous flow as they pass over a cold plate for atmospheric INP analysis. LOC-NIPI allows the user to define the number of droplets analysed by simply running the platform for as long as required. The use of small (~100 μm diameter) droplets minimises the probability of contamination in any one droplet and therefore allows supercooling all the way down to homogeneous freezing (around −36 °C), while a temperature probe in a proxy channel provides an accurate measure of temperature without the need for temperature modelling. The platform was validated using samples of pollen extract and Snomax®, with hundreds of droplets analysed per temperature step and thousands of droplets being measured per experiment. Homogeneous freezing of purified water was studied using >10 000 droplets with temperature increments of 0.1 °C. The results were reproducible, independent of flow rate in the ranges tested, and the data compared well to conventional instrumentation and literature data. The LOC-NIPI was further benchmarked in a field campaign in the Eastern Mediterranean against other well-characterised instrumentation. The continuous flow nature of the system provides a route, with future development, to the automated monitoring of atmospheric INP at field sites around the globe.

Introduction

Clouds are important to Earth's climate and energy budget due to their ability to reflect, absorb, and emit radiation, and their role in the hydrological cycle.[1–3] Clouds in the troposphere can exist as supercooled liquid droplets down to temperatures below about −33 °C before undergoing homogeneous freezing in the absence of nucleation sites.[4,5] Ice-nucleating particles (INPs) from a variety of sources, including desert dust, marine aerosols, and biological sources, can trigger heterogeneous freezing in supercooled liquid water clouds at higher temperatures.[6,7] The resultant ice crystals grow at the expense of the surrounding liquid droplets before falling out as precipitation, effectively removing the cloud or a portion of it. This can have a dramatic effect on the lifetime and radiative properties of clouds *via* complex cloud microphysical mechanisms, and in turn can have a profound effect on climate.[8] While many particles larger than ~100 nm can serve as cloud condensation nuclei (CCN), onto which water vapour condenses to form cloud droplets, only a tiny proportion can also serve as INPs. While CCN concentrations can frequently

---

[a] *School of Earth and Environment, University of Leeds, Leeds, LS2 9JT, UK. E-mail: m.d.tarn@leeds.ac.uk, b.j.murray@leeds.ac.uk; Tel: +44 (0) 113 343 5605, +44 (0) 113 343 2887*

[b] *School of Physics and Astronomy, University of Leeds, Leeds, LS2 9JT, UK. E-mail: j.shim@leeds.ac.uk; Tel: +44 (0) 113 343 3903*

[c] *Department of Earth and Planetary Sciences, Weizmann Institute of Science, Rehovot 76100, Israel*

† The data sets for this paper are publicly available in the University of Leeds Data Repository (https://doi.org/10.5518/847; Tarn *et al.* 2020).[187]

‡ Electronic supplementary information (ESI) available: Description of the thermocouple calibration procedure, the temperature control unit (Fig. S1), the experimental setup (Fig. S2), the characterisation of the cold plate (Fig. S3 and S4 and Table S1), details of the sampling times during the Eastern Mediterranean campaign (Table S2), and a discussion of the operational characteristics of the platform. See DOI: 10.1039/d0lc00251h

be in the range of 10^2 to 10^3 cm^{-3} in the mid-latitudes, the concentration of INPs that can trigger ice nucleation at, for example, −20 °C are typically only 10^{-4} to 10^{-2} cm^{-3}.

Heterogeneous ice nucleation in the atmosphere is thought to proceed *via* two main pathways: immersion mode, in which INPs are immersed within a liquid droplet, and deposition mode, in which water vapour deposits as ice onto an INP, and may involve liquid condensates in pores, which then freezes.[9,10] It has been suggested that immersion freezing may be the most common glaciation pathway in clouds containing supercooled liquid water.[11,12]

A range of instruments have been developed to study INPs in terms of their ice-nucleating activity and to measure their concentration in samples of air.[13–17] Two commonly used and complementary types of instruments are continuous flow diffusion chambers (CFDCs)[18] and cold stage-based droplet freezing assays.[19] CFDCs are online measurement instruments into which aerosols are continuously introduced and then flow between two ice-coated walls at different temperatures. These walls define the temperature and relative humidity that the aerosol is exposed to, allowing ice nucleation and crystal growth from INPs in the aerosol with subsequent detection of the ice crystals. Cold stage-based droplet freezing assays are commonly employed for immersion mode analysis in a batch format.[19–24] In these assays, droplets containing an aqueous suspension of INPs are arrayed on a cold stage and then cooled at a defined rate until all of the droplets have frozen. The droplet freezing temperatures can then be used to characterise the ice-nucleating activity of the INPs.

While CFDCs and cold stage-based droplet assays each provide information on INPs, they are complementary instruments, with each having their own advantages and disadvantages. As such, the two methods have been used side-by-side in a number of INP studies.[25–31] CFDCs can operate in immersion or deposition mode and can provide online measurements (*i.e.* direct sampling of aerosol) with high time resolution at lower temperatures. They have been deployed on aircraft,[32,33] as portable, field-deployable instruments,[34] as a commercial instrument,[35] and in an autonomous, semi-continuous monitoring fashion.[36] However, CFDCs are large, expensive, require significant infrastructure to run, cannot take measurements at warmer temperatures, and typically lack in sensitivity compared to cold stage-based droplet assays.[37,38]

In contrast, cold stage-based droplet freezing assay instruments are typically inexpensive, simple to construct, can be relatively small (*i.e.* benchtop), and are easy to operate by manually locating droplets onto a cold plate and cooling the plate. In addition, traditional droplet freezing assays often employ relatively large droplets (*e.g.* μL range), with the advantage that rarer INPs can be detected in the total droplet population at much warmer temperatures than possible with a CFDC. They can also be portable, provide lower detection limits and access warmer temperature regimes than CFDCs. As such, cold plate instruments have been adopted by many research groups. However, contemporary cold plate instruments have a number of distinct disadvantages. With the larger droplet volumes there is also an increased chance of impurities being present that cause nucleation at temperatures much higher than homogeneous freezing.[19] Further, the theory of homogeneous freezing implies that increasing the droplet size also decreases the time required for the first ice nucleus to form. These factors set the lower temperature limit for many droplet freezing assays, which for μL volume droplet freezing assays is many degrees above homogeneous freezing, meaning that these instruments are often blind to INPs below about −25 °C, although this has been pushed to temperatures approaching −30 °C in some exceptional cases.[22,39,40] In addition, they have only been applied to atmospheric INP analysis in an offline format, *e.g.* by analysing aerosol that has been collected *via* filters or impingers, and traditionally can only be run in a batch-based format of tens to hundreds of droplets per analysis. While the droplet arraying procedure can been automated,[41,42] it would be difficult to fully automate the entire procedure of a traditional droplet assay. For these reasons, an autonomous cold plate-based droplet assay platform has, thus far, not been developed for the continuous analysis of atmospheric INPs. However, microfluidics is a technology that offers high degrees of control, reproducibility and potential automation, and which may offer a route to addressing some of the deficiencies of traditional droplet freezing assays.

Recently, droplet microfluidic technology[43–51] has been explored for ice nucleation studies thanks to the ability to generate small, monodispersed droplets in the picolitre volume range, which can be manipulated within the on-chip environment and can be studied in their hundreds or thousands. The use of such small droplets reduces the probability of contamination by impurities,[19,52–62] allowing freezing assay baselines that can be far lower than those typically achieved using larger droplets. Droplet microfluidic ice nucleation instruments can routinely reach homogeneous nucleation, thereby extending the temperature range of INP measurements that can be obtained. Early droplet microfluidic studies focussed on homogeneous ice nucleation[63–67] and cryobiology,[67–69] but in the last few years a handful of examples have been applied to the study of atmospheric INPs.[24,41,42,70,71]

Most examples of microfluidic ice nucleation have involved the freezing of water-in-oil droplets in a static, batch system, akin to a traditional cold stage-based droplet freezing assay. This has been achieved using several methods, including: microfluidic traps to form arrays of droplets for on-chip freezing on a cryomicroscopy stage,[63,68,71–73] the microfluidic generation and collection of droplets for off-chip cooling,[66,67,70] the printing of droplets on a cold plate *via* a commercial piezo-driven droplet generator,[41,42] the arraying of droplets on a micropatterned surface atop a cold plate,[24] and the storage of droplets in a length of millifluidic tubing for in-tubing cooling.[74] While the above batch methods of microfluidic INP analysis are relatively straightforward and routinely provide low baselines, they suffer from some of the same disadvantages as traditional instruments using larger droplets. In particular, they are still limited in the numbers of droplets analysed per experiment, although hundreds of droplets are routine in microfluidic droplet assays compared to 10–100 in typical droplet freezing assays. Further, their implementation for autonomous, continuous monitoring would be difficult. A more convenient approach for a monitoring platform that could analyse as many droplets as desired would be to perform droplet freezing assays in continuous flow. While continuous droplet operations are commonplace in microfluidics,[46,47,75–81] there are only a handful of examples of performing ice nucleation in continuous flow.

Sgro *et al.*[69] demonstrated an early example of droplet freezing in flow using a Peltier element placed over or under a section of a chip, and used the setup to freeze droplet-encapsulated cells towards cryobiology applications. This required that the chip was simply cooled to a temperature that ensured the droplet population froze (at a Peltier element set temperature of −20 °C), and so the determination of droplet freezing temperatures was not performed. The temperatures inside the channel were modelled to provide information on the cooling rates, with water vitrification in mind, but no measurements of temperature in the flow within the chip were actually taken. This was appropriate for cryopreservation applications, but would not be appropriate for quantifying atmospheric INP concentrations.

Stan *et al.*[64] developed an elegant platform for ice nucleation experiments by employing a sequence of Peltier elements beneath a microfluidic device, allowing a thermal gradient to be generated across the length of the chip. As the droplets flowed through the channel, the position at which they froze was then related to the temperature at that location, determined *via* a combination of microfabricated thermometers in the channel and modelling. This continuous analysis platform was used to study the freezing of pure water droplets,[64] droplets containing silver iodide (AgI) particles to demonstrate heterogeneous freezing,[64] and the freezing of pure water in the presence of an electric field.[65] The platform demonstrated the potential of the continuous flow methodology for the study of ice nucleation, allowing tens of thousands of monodispersed droplets to be analysed with high temperature accuracy. However, the chip and the system comprised a complex fabrication and setup, including the use of seven co-controlled Peltier elements and the microfabrication of thermometers that required ∼100 electrical connections. A complication of this system was that, while the microfabricated thermometers allowed in-channel temperature measurement in the ceiling and the floor of the channel, a large temperature gradient to the centre of the channel necessitated modelling to determine the droplet temperature. Although an example of heterogeneous nucleation was demonstrated with AgI particles, the technique was not applied to the analysis of atmospheric INPs.[64,65] The ideal microfluidic system for studying atmospheric INPs, particularly in the field, would be relatively simple to set up and the droplet freezing temperatures would be characterised by a direct measurement rather than requiring modelling.

Here, we demonstrate a droplet microfluidics platform known as the LOC-NIPI (Lab-on-a-Chip Nucleation by Immersed Particle Instrument), for the analysis of atmospheric INPs in continuous flow. Droplets of aqueous suspensions of INPs are generated in fluorinated oil and passed over a cold plate on a cold stage platform to determine the number of droplets that freeze over a series of set temperatures (Fig. 1a), allowing the ice-nucleating activity of the INPs to be probed. The LOC-NIPI represents an advancement in cold stage droplet freezing assay instrumentation, offering many of the advantages of such assays with the benefits of a continuously flowing system, *i.e.* greater possible droplet numbers, lower baseline

(a) Principle of droplet freezing in flow

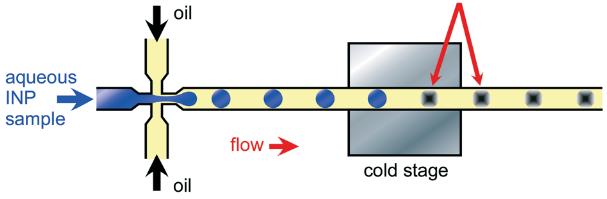

(b) Microfluidic chip design

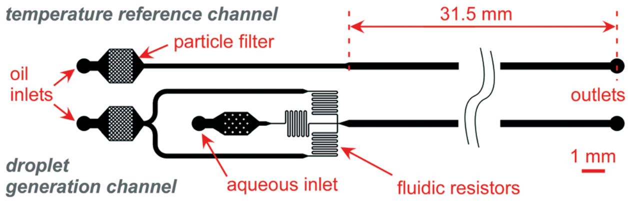

(c) Photograph of the microfluidic device

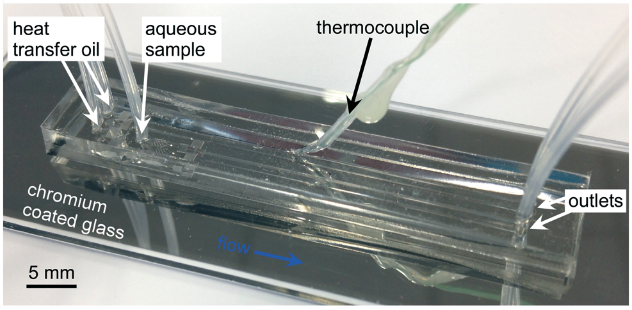

Fig. 1 Microfluidic droplet freezing in continuous flow *via* the LOC-NIPI (Lab-on-a-Chip Nucleation by Immersed Particle Instrument). (a) Schematic showing the principle of droplets freezing as they pass over a cold plate at a set temperature. (b) Channel design of the microfluidic device featuring two structures: a "droplet generation channel" (lower image) for the generation of water-in-oil droplets and their freezing in a 31.5 mm long channel, and a "temperature reference channel" (upper image) for monitoring the temperature of the flowing oil. (c) Photograph of the PDMS-on-glass chip, showing a thermocouple inserted into the temperature reference channel. The underside of the glass slide was coated with chromium to provide a reflective surface that enhanced the visualisation of droplet freezing events.

temperatures, and amenability to autonomous operation. A significant advantage of LOC-NIPI is that we eliminated the need for modelling of temperature in the flow channel by making temperature measurements with an insertable thermocouple probe,[82,83] making the system more easy to use by scientists in the field. The insertable probe was positioned in a reference channel in parallel to the droplet channel, thus providing a proxy measurement of the droplet temperature in a flowing system.

We view the LOC-NIPI as being a step towards an automated microfluidic apparatus for the immersion mode droplet assay-based measurement of INPs. The LOC-NIPI chips were designed to be simple and easy to fabricate, assemble, and operate in the field by non-microfluidicists. The LOC-NIPI has been tested using pure water and INP suspensions containing birch pollen extract or a freeze-dried form of *Pseudomonas syringae* bacteria (Snomax®), while field tests were performed during an aerosol sampling campaign in the Eastern Mediterranean.

Experimental

Chemicals

Fluorinated heat transfer oil, 3M™ Novec™ 7500 Engineered Fluid, was purchased from Fluorochem Ltd. (Hadfield, UK), and has a thermal conductivity range of 0.069 W m^{-1} K^{-1} at 0 °C to 0.075 W m^{-1} K^{-1} at −35 °C.[84] The fluorinated surfactant, Pico-Surf™ 1 (5% w/w in Novec™ 7500 oil), was purchased from Dolomite Microfluidics (Royston, UK) and Sphere Fluidics Ltd. (Cambridge, UK), and was further diluted to 2% w/w in Novec™ 7500 oil. Silicone oil was purchased from Sigma-Aldrich (Dorset, UK). Polyethylene glycol (PEG) was purchased from Fisher Scientific (Loughborough, UK). MicroChem SU-82075 was purchased from A-Gas Electronic Materials (Rugby, UK), while polydimethylsiloxane (PDMS, Dow Corning® Sylgard® 184 Kit) was obtained from Ellsworth Adhesives (East Kilbride, UK). Snomax® (lyophilised, non-viable *P. syringae*, manufactured by Snomax International, Englewood, CO, USA) was purchased from SMI Snow Makers AG (Thun, Switzerland). Silver birch pollen (*Betula pendula*, batch no.: BETP.0616, 2016 harvest) was purchased from Pharmallerga (Lixov, Czech Republic).

Preparation of Snomax® and birch pollen extract

Suspensions were prepared in purified water (18.2 MΩ cm at 25 °C, 0.22 μm filtered) obtained from a Sartorius Arium® pro water purification system.

A 0.1% w/w (*i.e.* 1 mg mL^{-1}) suspension of Snomax® was prepared in purified water and mixed by vortexing prior to experiments. Birch pollen (*B. pendula*) was prepared as described previously:[70,85] 1 g of dried pollen was suspended in 50 mL water (*i.e.* 2% w/v; 20 mg mL^{-1}) in a vial and shaken, then stored overnight in a fridge to settle. The solution was shaken again, then filtered through an 11 μm nylon net filter and a 0.2 μm cellulose acetate filter to give a suspension of pollen extract.

Microfluidic chip design

The microfluidic chip design was prepared using CleWin 5.2 Layout Editor software (WieWeb Software, Hengelo, The Netherlands) and featured two separate channel structures: the main channel for droplet generation and freezing of water-in-oil droplets in flow (lower design in Fig. 1b), and a single temperature reference channel that was used to measure the temperature of the flowing oil (upper design in Fig. 1b) as a proxy for the droplet channel.[82,83,86] The layouts were designed to have a channel depth of 140 μm following chip fabrication.

The droplet generation and freezing design consisted of a flow-focussing nozzle[87] for water-in-oil droplet production and a long main channel, designed to sit atop a cold plate, through which the droplets then passed to potentially freeze (Fig. 1b). The oil inlet channels split and diverged from a single initial oil inlet with the channels being of 200 μm width before narrowing to 40 μm as they converged to a flow-focussing nozzle for droplet generation A particle filter, comprising a chamber containing an array of narrowly spaced pillars (80 μm × 80 μm each), was located near to the oil inlet in order to capture any particles or fibres in the oil phase that might otherwise have flowed through the chip and clogged the flow-focussing nozzle.

The aqueous inlet channel also featured a filter, but with only a small number of widely spaced pillars to trap larger objects such as fibres without affecting the particles in the sample suspension. A short aqueous channel section of 180 μm width following the filter then narrowed to 40 μm prior to the flow-focussing junction. The 40 μm wide oil and water channels each contained a section of serpentine channel acting as a fluidic resistor to increase the flow resistance and to smooth out the fluid delivery from the syringe pumps, which otherwise may have caused pulsing at the given flow rates and affected the stability of the droplet generation and thus the monodispersity of the droplets.[88,89] The flow-focussing nozzle had a width of 40 μm, which thereafter expanded into a 300 μm wide, 31.5 mm long main channel wherein the droplets could be frozen.

The separate temperature reference channel design (the upper design in Fig. 1b) consisted of a single oil channel that contained a particle filter leading to a channel of 200 μm initial width that expanded into a width of 300 μm and a length of 31.5 mm to replicate the flow velocity in the main droplet channel design, thus allowing a temperature measurement of the droplet channel by proxy.

Microfluidic chip fabrication and setup

The microfluidic devices were fabricated in polydimethylsiloxane (PDMS) using standard soft lithography procedures.[90–92] Briefly, SU-82075 photoresist was spin-coated onto a silicon wafer (PI-KEM, Tamworth, UK), then the channel design exposed onto the resist *via* a direct laser writer (MicroWriter ML, Durham Magneto Optics Ltd., Caxton, UK). The wafer was then photodeveloped to leave only the exposed photoresist bearing the channel design structures on the surface, to a height of 140 μm, whereupon PDMS (10 : 1 base to curing agent) was poured onto the wafer and allowed to cure at 75 °C for 1 h. The PDMS was then peeled off the master, the individual microfluidic chips cut out with a scalpel, and 1 mm diameter access holes punched into each device. An extra 1 mm diameter hole was punched halfway along the temperature reference channel for insertion of the thermocouple probe, and was done so at a roughly 45° angle to allow ease of insertion, *i.e.* to avoid routing the thermocouple through a right-angle into the channel. The underside of the PDMS chips (*i.e.* the side with the imprinted channels) were sealed with 3 M™ Scotch Magic Tape until ready for bonding to a glass substrate. Glass microscope slides (76 × 26 × 1 mm^3, Academy Science Products, Kent, UK) were used as the lower substrate of the chips, and the underside of these were coated with a thin (~80 nm) layer of chromium *via* metal deposition (Edwards Auto 306 vacuum coating system) prior to bonding to provide a mirror finish that would enhance droplet visualisation during experiments. The PDMS device and the chromium-coated glass slides were treated with oxygen plasma (Zepto Version B, Diener Electronic GmbH, Germany) in order to promote bonding between the two substrates when they were then placed together and cured at 75 °C for 1 h to yield the final, sealed devices.[91]

Polyethylene tubing (Smiths Medical, 0.38 mm inner diameter (i.d.), 1.09 mm outer diameter (o.d.), Harvard Apparatus (Biochrom Ltd.), Cambridge, UK) was inserted into the inlet and outlet holes of a bonded device. The continuous phase (oil) tubing of both the main droplet generation channel and the temperature reference channel were interfaced to 1 mL glass syringes (SGE, Sigma-Aldrich, UK). The dispersed phase (aqueous suspensions) tubing of the main droplet generation channel was interfaced to disposable plastic syringes (1 mL, Henke-Sass Wolf, VWR, Lutterworth, UK) to avoid cross-contamination between samples. The two oil phase syringes were inserted into one syringe pump (PHD Ultra, Harvard Apparatus (Biochrom Ltd.), UK), while the single aqueous suspension syringe was inserted into a second syringe pump (PHD Ultra).

A thermocouple (80 μm diameter, ±2.2 °C, 5SRTC-TT-KI-40-1M series K-type, Omega Engineering Ltd., Manchester, UK), connected to a data logger (TC-08, ± 0.025 °C, Pico Technology, St. Neots, UK), was glued into either a polymer sleeve or a blunted syringe needle for ease of handling. The use of a sleeve or needle allowed the fast and simple insertion of the thermocouple into the access hole at the midpoint of the temperature reference channel such that the tip and a short section of thermocouple was inside the channel itself, with the sleeve providing a sufficient seal with the PDMS to prevent leakage. The relative dimensions of the thermocouple (having 80 μm diameter wires) to the microchannel cross-section (having a 300 μm × 140 μm cross-section) meant that the Novec™ 7500 oil could flow freely around it without any apparent effect on the fluid flow or backpressure. A photograph of a thermocouple inserted into a microchannel is shown in Fig. S3b in the ESI.‡

The calibration of the thermocouples is described in section 1 of the ESI.‡ The use of an insertable probe into the proxy temperature reference channel eliminated the need for the complex fabrication of integrated microfabricated temperature probes and modelling by the end user. Thus, the chip fabrication relies only on standard soft lithography procedures to manufacture the PDMS microfluidic devices from a mould, while the insertion and positioning of the thermocouple takes only a matter of seconds.

Cold stage platform

The cold stage platform was centred around three temperature-controlled plates on which the microfluidic chip would be placed. The platform was designed to be relatively simple to assemble, largely being comprised of commercial components in a 3D printed housing, and which could be connected to a temperature controller and to a standard recirculating chiller (set to a temperature of >0 °C). The platform was designed in SolidWorks (Dassault Systèmes SolidWorks Corporation, France) and consisted of a polymer housing comprised of four layers, which contained a series of three Peltier elements, liquid heat exchangers, and aluminium plates (see Fig. 2a for an exploded schematic of the platform, and Fig. 2b for a photograph of the assembled stage; the polymer housing layers are shown in green). The housing was 3D printed from the SolidWorks designs in Digital ABS Plus™ polymer (Stratasys, Derby, UK) using an Objet1000 Plus printer (Stratasys). The bottom layer of the housing (*i.e.* layer iv in Fig. 2a) contained three aluminium liquid heat exchangers (40 × 40 × 12 mm^3 water cooling block, Amazon, UK) in a row, with a wave spring washer placed beneath each block.

The next polymer layer up (*i.e.* layer iii in Fig. 2a) housed a three-tier Peltier element (Adaptive AP3-070-20-25 (3 W, 6.5 A, 6.5 V), Farnell, Leeds, UK) with an 8 × 14 mm^2 top tier that was located on the middle heat exchanger with a layer of thermal paste (Arctic Silver 5, Amazon, UK) to ensure good thermal contact. A machined aluminium block was placed on each of the two outer liquid heat exchangers, again with a layer of thermal paste. The top surface of each aluminium block was a 30 mm × 30 mm square, onto which a 30 × 30 mm^2 single-tier Peltier element (Adaptive GM250-127-10-15 (2.8 W, 0.59 A, 9.4 V), RS Components, UK) was thermal pasted.

The next polymer layer up (*i.e.* layer ii in Fig. 2a) contained three aluminium plates that were glued into it with Araldite Rapid epoxy resin, such that the plates sat flush with the upper polymer surface to provide a flat area onto which a microfluidic device would be placed. The middle aluminium plate was 8.4 × 14 × 3.7 mm^3, whilst the two outer plates were 37 × 33 × 2 mm^3. Each plate had a 1 mm diameter hole drilled through its side to its centre to allow the insertion of thermocouples for temperature

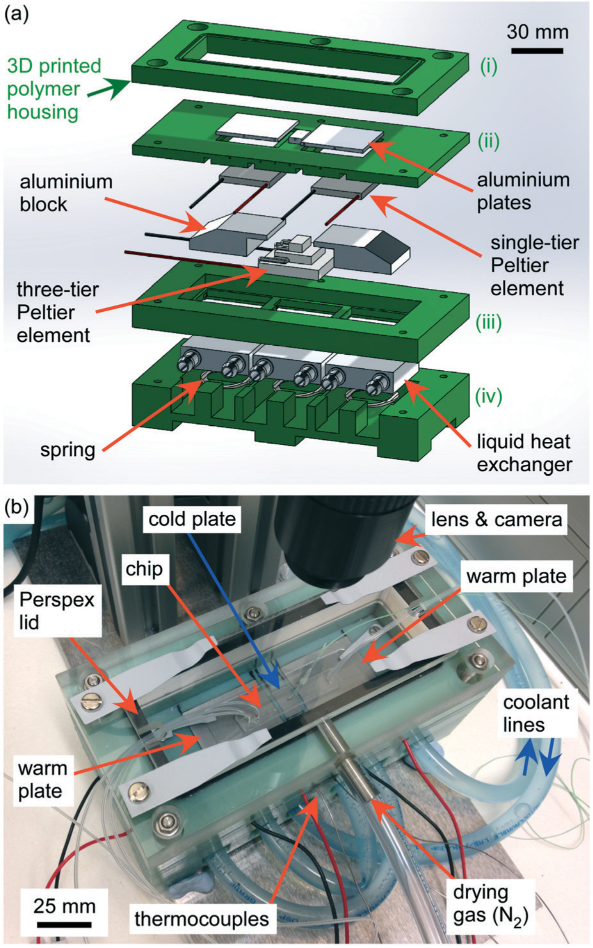

Fig. 2 Design and assembly of the cold stage platform used in the LOC-NIPI. (a) Exploded schematic of the platform, which used three Peltier elements to form warm and cold plates onto which a microfluidic device was placed. The housing of the platform was 3D printed in four layers of polymer (shown in green). (b) Photograph of the assembled cold stage platform with a microfluidic device located on the aluminium plates. The "quick access" Perspex lid is also shown. The microfluidic device is shown without a chromium coating to enable visualisation of the aluminium plates beneath.

measurements. This polymer layer was placed over the layer below such that the aluminium plates sat atop the three Peltier elements with thermal paste applied to ensure good thermal contact. The wave spring washers in layer iv ensured that the Peltier elements and aluminium blocks were pushed upwards against the three aluminium plates in layer ii, thereby ensuring good thermal contact. Sheathed thermocouples were inserted through the polymer layer and into the aluminium plates (406–532 thermocouples, K-type, 0.5 mm ∅ × 150 mm long, TC Direct), with thermal paste applied. The calibration of these thermocouples is described in section 1 of the ESI.‡

Polymer tubing (Thermo Scientific™ Nalgene™ 180 PVC, 1/4″ i.d., 3/8″ o.d., Fisher Scientific, Loughborough, UK) was used to link the liquid heat exchangers in layer iv together such that water would flow through each exchanger in turn, thereby actively cooling the warm side of the Peltier elements. The tubing layout ensured that water flowed first into the middle exchanger so that the three-tier Peltier element sitting beneath the main channel of the microfluidic device would receive maximum cooling, followed by the Peltier element that would be beneath the inlet of the microfluidic chip, and finally the Peltier element beneath the outlet of the chip. The inlet and outlet of the tubing was then connected to a refrigerated recirculating water chiller.

The top polymer layer of the platform (*i.e.* layer i in Fig. 2a) consisted of an open inner section, forming a perimeter with an embedded O-ring onto which a lid could be seated and sealed whilst providing space above the microfluidic chip for the inlet and outlet tubing, thus forming a chamber in which the experiments would take place. A Perspex lid was screwed into the top of layer i and sealed against the O-ring (Fig. 2b). The lid comprised a Perspex rim, into the edge of which was set a short section of stainless steel tube. This tube allowed dry gas to be introduced into the chamber *via* polyethylene tubing (Nalgene™ 180 PVC) to purge the platform of moisture, thus preventing condensation forming on the chip or the cold stage. The Perspex rim featured a shelf with a gasket onto which a removable Perspex insert could be placed in order to seal the chamber. The removable insert featured small gaps that allowed access for inlet and outlet tubing. The Perspex rim had clips attached to it that were used to lock the insert in place, providing quick access to the chamber of the platform. The platform also featured four small clips inside the chamber to hold the microfluidic chip in place.

When performing experiments on Snomax® and K-feldspar in the UK, water containing PEG was pumped through the liquid heat exchangers using a recirculating chiller set to 5 °C (WK 500, Lauda, UK), while compressed air was used to purge the cold chamber after first passing through a Drierite™ gas-drying unit (Sigma-Aldrich) and a particle filter (Whatman® HEPA-Cap 75, Fisher Scientific). When the cold stage platform was employed in the field campaign study in Israel, the liquid heat exchangers were supplied with water as a coolant *via* a refrigerated recirculating chiller set to 7 °C in order to cool the Peltier elements. Dry nitrogen (N_2) gas was used to purge the cold chamber through the tubing of the Perspex lid, with the N_2 gas supplied from a liquid nitrogen dewar.

Temperature control unit

To provide flexibility in the operation of the cold stage platform, a 4-channel temperature control unit was custom built in-house and consisted of a proportional-integral-derivative (PID) controller based on an Arduino Nano (purchased from RS Components, UK) microcontroller that allowed feedback-based temperature control of the cold stage platform *via* a program written in Python (Python Software Foundation, Delaware, USA). The Arduino Nano controlled four bi-directional motor drivers (IBT_2 BTS7960 43A High

Power Motor Driver) *via* a pulse width modulation (PWM) driver (PCA9685, Adafruit Industries, USA) that allowed the Peltier elements to be heated or cooled, while four K-type thermocouple amplifiers (AD8495, Adafruit Industries) connected to the Arduino Nano *via* an analog-to-digital converter allowed temperature measurements to be collected. Power was supplied to the Arduino Nano *via* a 12 V-to-5 V voltage converter. The temperature control assembly and the voltage converter were housed in a plastic enclosure (RS Components, UK) with ports allowing power cables (from the bi-directional motor drivers) and thermocouples (from the amplifiers) to be connected, in addition to a port to the voltage converter for power. Power was supplied from mains *via* a switching power supply (HEP-185-12A, Mean Well) that converted the 240 V AC mains supply to 12 V DC, and which was located external to the temperature control unit. A photograph of the electronics layout of the temperature control unit is shown in Fig. S1 in the ESI.‡

Three of the temperature control unit channels were employed here for the cold stage platform by connecting the power cables from the control unit to the three Peltier elements, and connecting the three thermocouples inserted into the aluminium plates of the cold stage platform to the control unit. The temperature of each aluminium plate could then be set individually and monitored using the Python program.

Visualisation setup

A modular Navitar Zoom 6000® Lens System (Mengel Engineering, Denmark) with a coaxial light port fed by an OPT Machine Vision 3 W light-emitting diode (LED) light source was used to visualise droplet freezing events in the chamber of the cold stage platform from a long working distance (~9.5 cm), through the clear Perspex lid. A Phantom Miro Lab 120 high-speed camera (Vision Research Ltd., Bedford, UK) was used to capture videos using PCC 2.7 (Phantom Camera Control) software (Vision Research Ltd.). Typically, around 90–200 seconds of video were collected during each droplet freezing experiment.

Freezing droplets in continuous flow

With the lid of the cold chamber open, a drop of silicone oil was placed on the aluminium plates of the cold stage platform, then a microfluidic device with a chromium coating on the glass underside was placed on the platform such that the droplet generation section and the inlet holes of the chip were located over one of the larger aluminium plates, with the outlet holes located over the other large aluminium plate. The tip of the thermocouple inside the temperature reference channel of the microfluidic chip was situated along the central line of the middle aluminium plate, *i.e.* the "cold plate". The silicone oil ensured good thermal contact between the chip and the aluminium plates; thermal grease could also be used but is more difficult to clean and replace when exchanging microfluidic chips. The lid of the cold chamber was closed, with the chip's inlet/outlet tubing and thermocouple fed through the gaps to access the syringes and data logger, respectively. The cold chamber was then purged with dry gas to remove moisture that would otherwise form condensation upon cooling of the chip. A photograph of the full experimental setup is shown in Fig. S2 in the ESI.‡

Droplets were generated in the droplet channel of the microfluidic device by pumping an aqueous sample and an immiscible fluorinated Novec™ 7500 oil (containing 2% w/w Pico-Surf™ 1 surfactant) into the chip *via* their respective inlets. As the two immiscible liquids entered the flow-focussing nozzle, the aqueous phase was squeezed between two streams of oil, allowing aqueous droplets to be pinched off.[48] Aqueous suspension was pumped into the chip at a flow rate of 0.02–0.1 μL min^{-1} and the Novec™ 7500 oil at a flow rate of 22–24 μL min^{-1}, unless otherwise stated. Droplets were produced with diameters typically around 80–100 μm, depending on the applied flow rates. Droplet generation rates were typically around 1–2 droplets s^{-1}, with velocities of around 11 mm s^{-1}.

Novec™ 7500 was used for the oil phase since it is a heat transfer fluid with a minimum working temperature of −100 °C,[84] and has a low viscosity at low temperatures that facilitates stable droplet production even when a portion of the liquid is held at temperatures of −35 °C. Conversely, attempts to use mineral oil at these temperatures led to difficulties in maintaining stable flow as the oil viscosity increased. Pico-Surf™ 1 fluorinated surfactant, a perfluoroether–polyethylene glycol (PFPE–PEG) block copolymer,[93,94] was employed in conjunction with the Novec™ 7500 oil since it enables the production of extremely stable and monodisperse water-in-oil droplets that can undergo temperature-based applications,[95–98] and which our group[70] and others[63,67] have previously employed for ice nucleation studies.

Novec™ 7500 oil was also pumped into the temperature reference channel, passing over the tip of the thermocouple probe at the same flow rate as in the droplet channel. This ensured that temperature measurements were more representative of the flowing liquid in the droplet channel than if a thermocouple had simply been inserted into the PDMS of the chip. Thus, the temperature recorded by the thermocouple probe in the reference channel was used as a proxy measurement for the temperature in the droplet channel. Details regarding the characterisation of the temperatures and their uncertainties are described in section 3 of the ESI.‡

During a droplet freezing experiment, the two aluminium plates beneath the inlet and outlet sections of the microfluidic chip were held at +3 °C, thus ensuring that the water entering the chip did not freeze prior to droplet production and that any frozen droplets in the chip would melt before exiting, and so would be unable to block the flow. Holding the inlet section of the chip at a set temperature also prevented significant changes in generated droplet size that can occur when droplets are produced at different temperatures under otherwise identical operational conditions.[99]

The temperature of the middle "cold plate" was reduced below 0 °C and held at a set temperature (with a typical variation of about 0.03 °C) to allow around 90–200 s of video to be recorded of droplets as they passed through the microchannel, corresponding to around 0.08–0.17 μL of aqueous sample. The temperature was then reduced (with the increment depending on the experiment; details are provided in the relevant sections in the Results and discussion) and the procedure repeated to span the desired temperature range, providing a number of videos that each showed a population of droplets traversing the channel at a different sub-zero temperature. Although the temperatures used during these experiments were applied by setting the cold plate temperature, the temperatures used for data analysis were taken from the thermocouple inserted into the microfluidic device. The amount of time required for the temperature to stabilise in the chip upon changing the cold plate set temperature depended on that set temperature, with the longest time being a few minutes at the lowest temperatures, although this could be sped up by decreasing the temperature of the recirculating chiller used to cool the Peltier elements. The timeframe to complete each set of experiments varied depending on the number of temperature increments investigated and the number of droplets analysed per increment, but most experimental runs discussed here took around 60–90 min.

Droplet counting and the determination of freezing events from recorded videos were achieved manually, with hundreds of droplets typically analysed per temperature setpoint and so thousands of droplets per experiment. Future iterations of the system will include development and implementation of an automated droplet freezing analysis program, similar to those demonstrated by other groups for image analysis in their droplet assay techniques.[21,64,66,71,73] The droplet diameters, droplet production rates, and droplet velocities were calculated using PCC 2.7 software. The measurement resolution when determining droplet diameters was 6 μm per pixel due to the low magnification used when recording videos, which was selected in order to achieve a wide field of view and observe droplets as they traversed the entire width of the cold plate. This error could be reduced in future by using a higher magnification during experiments.

The estimated temperature errors determined from these results were between ±0.4 °C and ±0.7 °C depending on the on-chip temperature range, as detailed in Table S1 of the ESI.‡ The platform was designed such that the droplets experienced a high initial cooling rate upon first entering the cold region, before passing over an isothermal region at the centre of the cold plate where the droplet freezing measurements were taken (see the discussion in section 3 of the ESI‡ and in Fig. S4). As droplets first entered the region of the microchannel directly above the cold plate, the initial cooling rates ranged from 200 °C min^{-1} (0.3 °C mm^{-1} along the channel) to 2400 °C min^{-1} (3.3 °C mm^{-1}) depending on the cold plate temperature (0 to −39 °C). Within the isothermal region of the microchannel over the cold plate, the droplets were estimated to experience a temperature variability of ±0.2 °C for ∼0.2 s.

The platform was tested using (i) purified water, (ii) a 0.1% w/w (1 mg mL^{-1}) suspension of Snomax® (non-viable *P. syringae*), (iii) an extract prepared from a 2% w/v (20 mg mL^{-1}) suspension of silver birch pollen (*B. pendula*), and (iv) was applied to the measurement of field samples collected and analysed in the Eastern Mediterranean. A new chip was used for at least each different sample type as a precaution against contamination, although there did not appear to be any evidence of contamination once a chip had been thoroughly washed with purified water between experiments.

Comparison to conventional droplet assay technique

The lab-prepared INP standards (0.1% w/w Snomax® and 2% w/v birch pollen extract) were analysed using a conventional 1 μL droplet assay technique, the Microlitre Nucleation by Immersed Particle Instrument (μL-NIPI),[20] for comparison to data obtained using the LOC-NIPI. The μL-NIPI has been used extensively in the literature and has been involved in multiple intercomparison studies,[13,15,17] hence it provides a useful benchmark for the LOC-NIPI.

Here, 40–50 droplets (1 μL volume each, ∼1.5 mm diameter) of aqueous INP suspension were pipetted onto a hydrophobic glass slide (22 mm ⌀ × 0.22 mm siliconised glass cover slides, Hampton Research, Aliso Viejo, CA, USA) atop a Stirling engine-based cold stage (EF600, Grant-Asymptote Ltd., Cambridge, UK). A Perspex shield was placed over the glass slide to form a chamber, which was then purged with a flow of dry nitrogen (N_2) gas to prevent condensation forming as the cold stage was cooled at a rate of 1 °C min^{-1} to −40 °C. Videos of the droplets freezing were recorded as the temperature was reduced, and synchronisation with the cold stage temperature measurements allowed the droplet freezing temperatures to be calculated.

Aerosol analysis in the Eastern Mediterranean

Atmospheric aerosol samples were collected at the Weizmann Institute of Science in Rehovot, Israel (31.9° N, 34.8° E; ∼80 metres above sea level (m a.s.l.)). Samples were obtained using two sampling strategies: (i) the collection of aerosol particles onto filters, and (ii) the sampling of aerosols directly into water using an impinger. Purified water (18.2 MΩ cm at 25 °C, 0.22 μm filtered) was used for preparing the particle suspensions in both cases and was obtained using a Thermo Scientific™ Barnstead™ GenPure™ water purification system.

Filter-based sampling was performed using our previously employed methodology,[100] in which a BGI PQ100 Air Sampling System with a PM_{10} (particulate matter with diameters ≤10 μm) inlet (Mesa Laboratories, Lakewood, Colorado, USA) was used to pull air through a thin, porous filter onto which the particles were adsorbed. The BGI PQ100 was designed to Environmental Protection Agency

(EPA) requirements and is used as an EPA Reference Method for PM_{10} (designation no. RFPS-1298-124). This allowed the sampling of PM_{10} onto Whatman® Nuclepore™ track-etched membrane polycarbonate filters (47 mm diameter, 1.0 μm pore size, Sigma-Aldrich, UK) at 16.67 L min^{-1} (1 m^3 h^{-1}). Two filter-based samples were analysed using the microfluidic platform, which were collected for 3 h (14:28 to 17:28 on 31st October 2018; 3000 L of air) and 24 h (11:45 on 25th October 2018 to 11:45 on 26th October 2018; 24 000 L of air), respectively. Although the filters had a 1.0 μm diameter pore size, such filters can collect particles across the full size range with high efficiency, including particles much smaller than the pore size.[101,102] Following sampling, the filter was removed from the system and inserted into a 50 mL centrifuge tube (Sarstedt Ltd., Leicester, UK) using tweezers, then 4 mL of purified water added. The tube was shaken vigorously and then vortexed for 5 min using a vortex mixer (Labnet VX100) to wash the particles from the filter into suspension. The 3 h sample was analysed immediately, while the 24 h sample was frozen for 7 days before being thawed and analysed in order to prevent the change or growth of biological material that could influence the apparent INP concentrations.[103]

Impinger-based sampling was achieved using a Bertin Technologies Coriolis® Micro air sampler (Air Monitors, UK), which aspirates air into a liquid-filled cone to form a vortex, allowing particles to be centrifuged to the wall of the cone and thus extracted from the air and into the water. One sample obtained *via* the impinger was used for microfluidic analysis, which was obtained with 20 min of sampling (collected in two 10 minute periods of 15:09–15:19 and 15:23–15:33) on 3rd November 2018 at a flow rate of 300 L min^{-1} (18 m^3 h^{-1}; 6000 L of air). The cone was initially filled with 15 mL water, then 6 mL added following the first 10 min sampling period due to evaporative losses. Following the second 10 min sampling period, the cone's contents had a mass of 4.98 g (≈4.99 mL). The cone was vortexed for 5 min on a vortex mixer (Labnet VX100) shortly after sampling to resuspend the particles in the water, then stored in a fridge until ready for use. The cone was then vortexed again immediately prior to analysis to ensure suspension of the particles. The collected filter-based and impinger-based aerosol samples were also analysed using the conventional μL-NIPI technique, as described above. An optical particle counter (OPC; Model 1.109, GRIMM Technologies) was also used to monitor the ambient total aerosol concentrations in the 0.25–32 μm size range throughout the campaign.

Further samples were collected independently during the field campaign using a micro-orifice uniform deposition impactor (MOUDI), and then analysed using the batch microfluidic "WeIzmann Supercooled Droplets Observation on a Microarray" (WISDOM) droplet freezing assay instrument.[71] WISDOM has previously been employed for the analysis of the ice-nucleating activity of size-resolved desert dust aerosol in the local region,[71,104] time-dependent freezing,[105] secondary ice processes in clouds,[106] the study of antifreeze proteins,[107] and the study of ice-binding proteins.[108] Briefly, samples were collected onto polycarbonate filters for ∼8 h and washed into suspension using water. A microfluidic array of 100 μm diameter droplets was formed on the WISDOM, which was cooled at 1 °C min^{-1} and the freezing events observed. This allowed some comparison of detected INP concentrations between the LOC-NIPI and the WISDOM, two microfluidic platforms that operate in similar droplet size and temperature ranges but in different manners (*i.e.* continuous flow *vs.* static array), although the exact aerosol sampling times varied between the instruments.

Theory

Ice-nucleating particle analysis

LOC-NIPI results were obtained by recording videos of droplets flowing over the cold plate for a series of set temperatures. Droplet freezing events were identified through a colour change in the droplet (Fig. 3). When nucleation occurs in a droplet, it is accompanied by the immediate dendritic growth of ice to the outer edges of the droplet, thus generating a number of liquid–ice interfaces that alter the light scattering properties of the droplet, causing it to appear black under the lighting conditions applied here.[21,64,70,71] Once the entire droplet has frozen and become a single ice crystal, it no longer has the multiple liquid-ice interfaces and so becomes transparent again.

The fraction frozen of the total droplet population, $f_{\text{ice}}(T)$, at temperature T in each recorded video was calculated using eqn (1):[19,109–112]

$$f_{\text{ice}}(T) = \frac{n_{\text{ice}}(T)}{n_{\text{tot}}} \tag{1}$$

where $n_{\text{ice}}(T)$ was the number of droplets frozen and n_{tot} was the total number of droplets in the video. Further analysis was performed by applying a singular approximation, in which it is assumed that (i) ice nucleation is temperature-dependent and time-independent, (ii) that each droplet containing INPs freezes at a characteristic temperature that depends on the nature of the INPs, (iii) the freezing of a droplet occurs due to a single nucleation event, and (iv) that each droplet contains the same average surface area of particles. On many materials, nucleation is both a site-dependent and a time-dependent process,[105,113,114] and there are methods for accounting for both dependencies simultaneously.[111,115,116] However, for simplicity we chose to make the approximation that time-dependence is second order,[113,114] and hence report active site densities as described below.

Using the singular approximation, the cumulative number of ice nucleation sites per unit volume of water, $K(T)$, at temperature T was calculated from $f_{\text{ice}}(T)$ and the droplet volume, V:

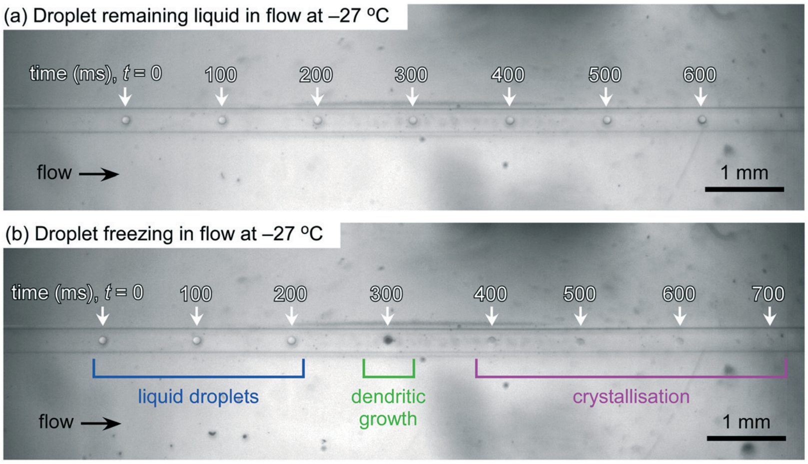

Fig. 3 Superimposed photographs showing (a) a single droplet as it passes through the microfluidic channel at −27 °C and remains liquid, and (b) a single droplet as it traverses the channel at −27 °C and freezes partway along the channel. The dendritic growth of an ice crystal following nucleation can be seen at 300 ms (from the initial on-screen appearance of the droplet) in (b), with the droplet becoming black during this growth phase before fully crystallising into an ice crystal within a further 100 ms. The fraction frozen, $f_{\text{ice}}(T)$, for this sample at −27 °C was 0.17, meaning that 17% of the droplet population froze at that temperature.

$$K(T) = \frac{-\ln\left(1 - f_{\text{ice}}(T)\right)}{V} \tag{2}$$

If the mass concentration, C_{m}, of the INPs in the particle suspension is known, $K(T)$ can be used to determine the active site density (*i.e.* the number of ice nucleation active sites) per mass of INPs, $n_{\text{m}}(T)$, the active site density per surface area, $n_{\text{s}}(T)$, or the active site density per particle, $n_{\text{n}}(T)$:

$$\frac{K(T)}{C_{\text{m}}} = n_{\text{m}}(T) = n_{\text{s}}(T)\cdot A = n_{\text{n}}(T)\cdot N \tag{3}$$

where A is the surface area of INPs per droplet, and N is the number of particles per sample mass. Normalising INP activity to these active site density values allows the comparison of INP results between different instruments, as highlighted in several intercomparison studies between a range of platforms,[13–17] in addition to providing an indication of a material's ice-nucleating ability. We note that we only normalise our Snomax® and pollen extract data in terms of $n_{\text{m}}(T)$ here, since details on A and N were not readily available, but have shown the various expressions in eqn (3) to demonstrate the relationship between different features of an INP population.

Fraction frozen data obtained from aerosol samples can also be used to calculate atmospheric INP concentrations, $[\text{INP}]_T$, in terms of the number of INPs per litre of sampled air:

$$[\text{INP}]_T = \frac{-\ln\left(1 - f_{\text{ice}}(T)\right)}{V} \cdot \frac{V_{\text{wash}}}{V_{\text{air}}} \tag{4}$$

where V is the droplet volume, V_{wash} is the volume of water used to wash the particles off the collection filter and into suspension (*i.e.* 4 mL), and V_{air} is the volume of sampled air.

Results and discussion

Homogeneous freezing of purified water

Experiments with droplets of purified water were run on the LOC-NIPI platform in order to study the homogeneous freezing of water. The fraction frozen ($f_{\text{ice}}(T)$) data from three pure water tests, run at slightly different flow rates, are shown in Fig. 4. Results for Snomax® and pollen extract are also shown in Fig. 4 but will be discussed in later sections, though we note here that there is no expectation that the LOC-NIPI and μL-NIPI results would be comparable prior to normalisation to a common factor (see eqn (2) and (3)).

The sample run at flow rates of 0.05 μL min^{-1} and 22 μL min^{-1} for the water and oil, respectively, was studied at 0.1 °C temperature increments on the cold plate, and 200 s long videos were collected at each temperature for analysis. With 403 ± 116 droplets (84 ± 7 μm diameter (coefficient of variation, CV = 8%), 311 ± 76 pL volume, 10.9 ± 0.1 mm s^{-1} droplet velocity) analysed per video and thus per data point on the $f_{\text{ice}}(T)$ plot, the entire dataset for this one sample comprised 10 881 droplets (equivalent to ∼3.4 μL of water in total). Shorter videos were collected for the other two samples, with 3692 droplets analysed in total for one (water flow rate = 0.02 μL min^{-1}, oil flow rate = 24 μL min^{-1}; 89 ± 7 μm diameter (CV = 8%), 371 ± 85 pL volume; 11.9 ± 0.1 mm s^{-1} droplet velocity; 0.1 °C temperature increments; 217 ± 48 droplets per data point), and 1833 droplets analysed for the other (water = 0.05 μL min^{-1}, oil = 24 μL min^{-1}; 85 ± 7 μm diameter (CV = 8%), 317 ± 73 pL volume; 11.9 ± 0.1 mm s^{-1} droplet velocity; 0.2 °C temperature increments; 167 ± 62 droplets per data point).

The three separate runs compared very well with each other, with freezing of the pure water droplet populations occurring in the range of −35.1 °C to −36.9 °C, below which all of the droplets were frozen. In order to compare the data to the literature to establish whether the pure water droplets

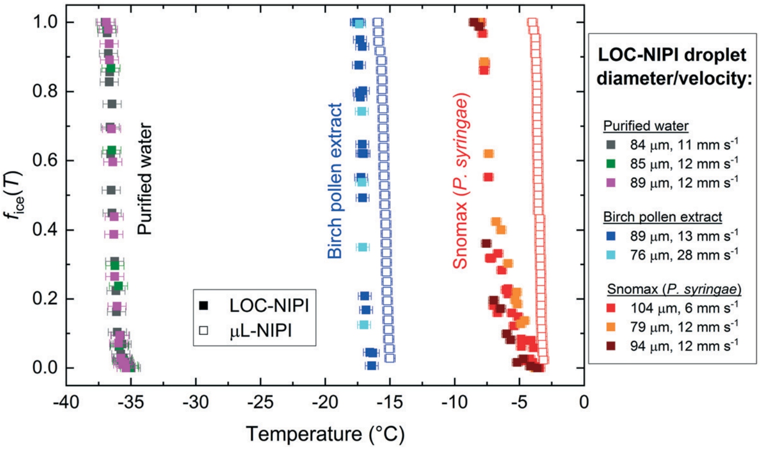

Fig. 4 Plot showing the fraction of droplets that froze out of a given droplet population, $f_{ice}(T)$, over a range of temperatures for purified water, silver birch pollen extract, and Snomax®. The solid squares represent data obtained using the microfluidic LOC-NIPI platform, while the open squares represent data obtained using the μL-NIPI, a conventional 1 μL droplet array system. The average diameters and velocities of the droplets for each set of LOC-NIPI results are shown in the legend on the right.

were likely to freeze homogeneously, we calculated the volume nucleation rate coefficient, $J_V(T)$, *i.e.* the number of ice nucleation events per unit volume per unit time, during the time period, Δt:

$$J_V(T) = \frac{-\ln(1-f_{ice}(T))}{V\Delta t} \quad (5)$$

Eqn (5) arises from the assumption that the ice nucleation rate coefficient can be related to observed droplet freezing events *via* a Poisson statistics, and detailed descriptions of this relationship are provided by Atkinson *et al.*[117] and Vali.[19] Here, eqn (5) was applied to each of the three purified water datasets, with the value of Δt calculated for each dataset depending on the time taken for a droplet to pass over a portion of the cold plate at which the temperature was coldest and relatively consistent (within 0.2 °C). Based on temperature characterisation tests (see section 3 of the ESI‡), it was estimated that a region of about 1.5 ± 0.5 mm in the centre of the cold plate was within ±0.2 °C, which, given a droplet velocity of 11.6 ± 0.6 mm s^{-1}, yielded a Δt of 0.13 ± 0.01 s. The $J_V(T)$ results for the three experimental runs are plotted in Fig. 5a and provided a fit of: $\log J_V(T) = -1.83047x - 59.42959$, in the range of −35.1 °C to −36.9 °C. The R^2 value was 0.95962, the upper $J_V(T)$ error was +87% of the $J_V(T)$ values, the lower $J_V(T)$ error was −43% of the $J_V(T)$ values, and the temperature error was ±0.73 °C.

The relatively large $J_V(T)$ error was a result of using a low microscope magnification in order to obtain a wide field of view, which in turn yielded a 6 μm per pixel measurement resolution during analysis of the droplet diameters. Propagation of this uncertainty thus presents a large standard deviation when calculating the droplet volume from its diameter, in turn affecting the calculation of $J_V(T)$. Furthermore, the upper uncertainty includes the values of $J_V(T)$ assuming that a distance of only 1 mm of the centre of the cold plate had a temperature variation within ±0.2 °C, while the lower uncertainty includes the values of $J_V(T)$ assuming that 2 mm of the cold plate centre had a variation within ±0.2 °C.

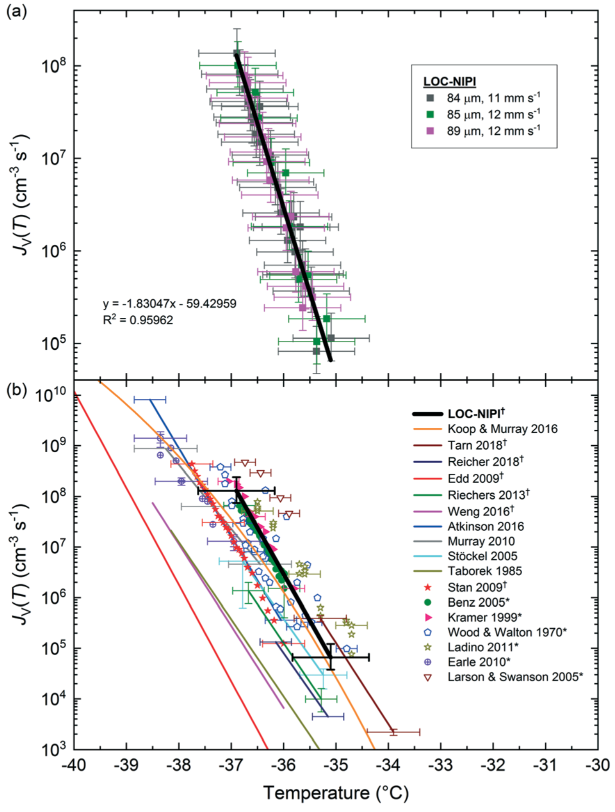

Fig. 5 Plots showing the volume nucleation rate coefficient, $J_V(T)$, of purified water. (a) Results from multiple runs using the LOC-NIPI, with a linear fit applied to the data. Average diameters and velocities of the droplets are provided in the legend. (b) Comparison of the LOC-NIPI fit to literature data.[63,64,66,67,70,71,117–127] Literature parameterisations are shown as solid lines while individual data points represent raw data. Data obtained *via* plot digitisation are indicated with *, while microfluidic data are indicated with †. Only a handful of error bars are shown for clarity.

Fig. 5b shows the LOC-NIPI $J_V(T)$ fit compared to data in the literature,[117–127] including data from other microfluidic techniques.[63,64,66,67,70,71] Microfluidic data are indicated with the symbol: †, while data obtained by digitising plots in the literature are indicated using the symbol: *. The LOC-NIPI data fell within the bulk of the datasets, including the more recent microfluidic data. In particular, the LOC-NIPI results fit well with the recent parameterisation by Koop and Murray,[118] which was based on a physically constrained version of classical nucleation theory (CNT), although the LOC-NIPI $J_V(T)$ values were slightly higher at lower temperatures and did not follow the slight curve of the Koop and Murray parameterisation. Given these excellent comparisons, we are confident that our data, obtained from >15 000 droplets in total, was in the homogeneous freezing regime and that the LOC-NIPI can provide excellent background signals when performing INP analysis.

Snomax® (biological ice nucleant)

Snomax® is a commercially available form of the Gram-negative bacterium, *P. syringae*, that has been rendered non-viable and lyophilised, and which is used in the production of artificial snow.[128] *P. syringae* is a plant pathogen[129–131] containing the *ina* (ice nucleation active) gene that confers upon it exceptional ice-nucleating properties.[14,131–140] *P. syringae* is present in the atmosphere[134,141–144] and has been found in precipitation[131,140,145–147] and cloud water,[148] although there is some debate over whether it, and other biological INPs, are present in high enough concentrations to be atmospherically important compared to mineral dusts.[141] Due to its excellent efficiency as an INP, Snomax® is commonly used as a test substance for ice nucleation equipment or to test hypotheses,[21,22,24,67,70,149–151] and has been used in instrumental/institutional intercomparison studies.[14]

Here, a 0.1% w/w (*i.e.* 1 mg mL^{-1}) suspension of Snomax® was analysed using the LOC-NIPI to validate its applicability to the study of INPs. The same Snomax® suspension was analysed in three separate runs at three sets of flow rates, in addition to analysis using the μL-NIPI platform, which employs a conventional 1 μL droplet assay, for comparison. The $f_{\mathrm{ice}}(T)$ results for Snomax® are shown in Fig. 4, and we note that, prior to any normalisation of the data to a common factor (such as mass or surface area of nucleant), there is no expectation that the μL-NIPI data would match the LOC-NIPI data. The temperature error for the LOC-NIPI data was ±0.4 °C, while the error for the μL-NIPI data was ±0.4 °C. The LOC-NIPI data fell in the temperature range of −3.5 °C to −7.9 °C. While the μL-NIPI data was composed of 44 droplets, and therefore 44 data points in total, each data point in the LOC-NIPI data comprised 282 ± 110 droplets, with a total of 11 450 droplets having been analysed in the data shown. Given the nature of the LOC-NIPI setup, each experiment yields a single data point that is independent of data points around it, hence the scattered nature of the data in the plot. This is in contrast to conventional droplet freezing assays in which the $f_{\mathrm{ice}}(T)$ data are calculated cumulatively, yielding a curve of data points rather than a scatter.

Two of the experimental runs were performed at similar flow rates that yielded similar droplet velocities: one exhibited a droplet velocity of 11.9 ± 0.2 mm s^{-1} (79 ± 7 μm droplet diameter (CV = 9%); 263 ± 68 pL droplet volume, oil flow rate = 22 μL min^{-1}, aqueous suspension flow rate = 0.05 μL min^{-1}), and the other a droplet velocity of 11.7 ± 0.2 mm s^{-1} (94 ± 7 μm droplet diameter (CV = 7%); 432 ± 96 pL droplet volume, oil flow rate = 22 μL min^{-1}, aqueous suspension flow rate = 0.1 μL min^{-1}). However, a third run was performed with around half the droplet velocity of 5.5 ± 0.1 mm s^{-1} (104 ± 7 μm droplet diameter (CV = 6%); 586 ± 113 pL droplet volume; oil flow rate = 1 μL min^{-1}, aqueous suspension flow rate = 0.05 μL min^{-1}), in order to test whether the freezing characteristics were influenced by flow rate and therefore the velocity at which the droplets pass over the cold plate. Based on the results here, the velocity of the droplets through the chip did not have a notable effect at the flow rates tested.

The ice-active site density per unit mass, $n_m(T)$, for the LOC-NIPI and μL-NIPI was calculated by normalising the $f_{\mathrm{ice}}(T)$ data to the droplet volume and Snomax® concentration, as per eqn (2) and (3), and the results are shown in Fig. 6a. The temperature errors were the same as for the $f_{\mathrm{ice}}(T)$ data in Fig. 4, whilst the $n_m(T)$ errors were calculated based on uncertainties in droplet volume and weighing errors. The $n_m(T)$ errors also incorporated Monte Carlo simulations to estimate the uncertainty due to the random distribution of ice-active nucleation sites for each droplet freezing experiment, as described previously.[70,152,153] The plot demonstrates the complementarity of the LOC-NIPI and μL-NIPI data, with the former providing an extension of the latter into lower temperatures.

This same $n_m(T)$ data are also plotted against literature data for Snomax® in Fig. 6b for comparison,[6,14,21,22,67,137,149,150,154] including against available microfluidic data (indicated with the symbol: †).[24,67,70,73] Data for strains of *Pseudomonas* bacteria,[6,137,154] rather than Snomax®, are indicated with the symbol: ‡. Data that was obtained by digitising plots from the literature is indicated with the symbol: *.

The LOC-NIPI data compares very well with the available literature, particularly in that it falls on the fit by Wex *et al.*[14] that was calculated from the results of an intercomparison study. The results also fit well with several other studies, even to the extent of demonstrating similar degrees of variation in repeat measurements, such as in Budke and Koop,[21] Polen *et al.*,[150] and the experimental data shown by Wex *et al.*[14] The LOC-NIPI data also followed the characteristic S-shaped curve exhibited by much of the literature data.

It is known that the ice-nucleating activity of Snomax® degrades over time, with significant reductions occurring within months of storage.[150] The Snomax® sample used here was received from the supplier around 2 months prior to

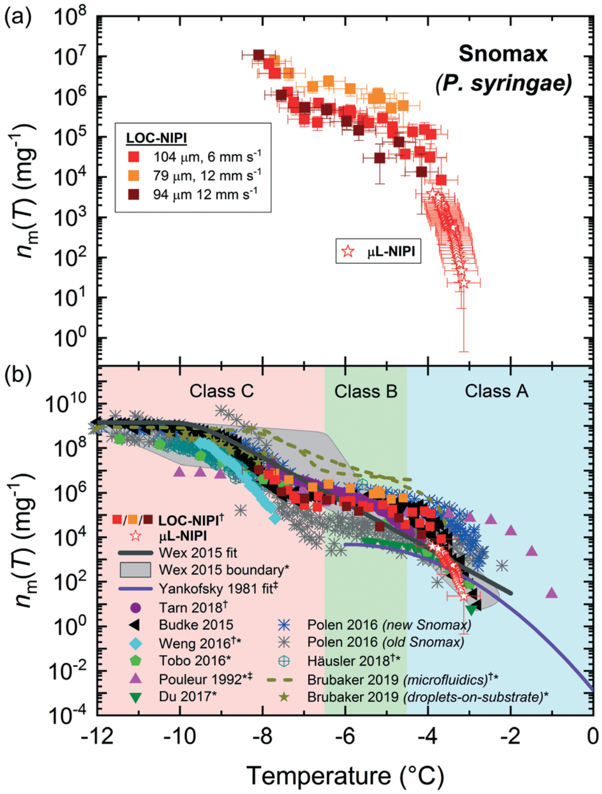

Fig. 6 Plots showing the active site density per mass of Snomax®, a non-viable, lyophilised form of *P. syringae*. (a) Results obtained using the microfluidic LOC-NIPI platform (■) and the conventional μL-NIPI technique (☆), including error bars on each data point. The average diameters and velocities of the droplets are provided in the legend. (b) Comparison of the LOC-NIPI and μL-NIPI results to literature data,[6,14,21,22,24,67,70,73,137,149,150,154] with only a handful of error bars shown for clarity. Microfluidic data are indicated with †, digitised data from the literature are indicated with *, and data for *Pseudomonas* strains (*i.e.* not in the form of Snowmax®) are indicated with ‡.

experiments, and was stored in a freezer during that time to reduce the degradation. Thus, the LOC-NIPI results are closer to the Polen *et al.*[150] data for "new" Snomax® than for the "old" Snomax®, as expected given that the Snomax® was relatively new. It is also worth noting that the ice-nucleating ability of Snomax® is denoted by its classification into three categories corresponding to different-sized aggregates of ice-nucleating proteins associated with *P. syringae*: class A, which are active at $\gtrsim -4.5$ °C; class B, which are active at ≈ -4.5 °C to −6.5 °C; class C, which are active at $\lesssim -6.5$ °C. Thus, it can be seen in Fig. 6b that the Snomax® analysed using the LOC-NIPI comprised all three types, with the class A activity likely being available due to the Snomax® being relatively new.

In summary, the LOC-NIPI results for Snomax® demonstrated excellent correlation with the μL-NIPI results and with the multitude of literature data, including the variation in signal that can be observed in several datasets in which multiple analyses have been performed. The temperature of the flowing liquid was used to plot the data rather than the cold plate temperature, and changes in flow rates did not appear to affect the results. Given the scatter observed in the Snomax® data from both the LOC-NIPI and the rest of the community, we wished to evaluate the LOC-NIPI using an INP population with a narrow range of freezing temperatures, and so chose to analyse pollen for a second series of INP tests.

Birch pollen extract (biological ice nucleant)

Pollen is an effective biological ice nucleator,[85,155–157] albeit less active than *P. syringae*/Snomax®, and is known to be present in the atmosphere,[134,144,158,159] although its impact on ambient INP concentrations is under debate.[160] Pollen grains can contain thousands of ice-nucleating (and ice-binding) polysaccharides bearing carboxylate groups[155,157] that are released upon contact with water.[156,160]

The LOC-NIPI platform was further tested using an extract (filtered to 0.2 μm) of wild silver birch pollen (*B. pendula*) from a 2% w/v (*i.e.* 20 mg mL^{-1}) suspension, which has been analysed in previous literature and typically yields a very narrow range of freezing temperatures.[24,70,85,155,156] The same extract was analysed using the μL-NIPI, and the $f_{\text{ice}}(T)$ data for both the LOC-NIPI and μL-NIPI are shown in Fig. 4. The temperature error was ±0.5 °C for the LOC-NIPI, and ±0.4 °C for the μL-NIPI.

Two runs were performed using the LOC-NIPI at two sets of flow rates that provided two different droplet velocities. One of these used the standard flow rates of 22 μL min^{-1} for oil and 0.05 μL min^{-1} for the aqueous pollen extract, yielding a droplet velocity of 12.8 ± 0.3 mm s^{-1} (89 ± 7 μm diameter (CV = 8%); 371 ± 84 pL volume; 420 ± 59 droplets per data point; 6720 droplets in total). The other run, however, used flow rates of 44 μL min^{-1} for the oil and 0.2 μL min^{-1} for the pollen extract in order to determine the effect of roughly doubling the droplet velocity to 28.4 ± 0.6 mm s^{-1} (76 ± 7 μm diameter (CV = 9%); 234 ± 66 pL volume; 620 ± 41 droplets per data point; 3102 droplets in total), and whether the LOC-NIPI could still freeze droplets at such high speeds. The LOC-NIPI droplet freezing temperatures ranged between −15.0 °C and −17.1 °C. The results from both sets of flow rates showed excellent comparison (see Fig. 4 and 7a), indicating that the temperature measurements were valid even at the much higher set of flow rates. This shows promise for increasing the droplet throughput further without affecting the droplet freezing characteristics, although this would need to be confirmed *via* testing and with consideration to other affected aspects, *e.g.* increased droplet cooling rates.

The ice-active site density per gram of pollen in the original suspension, $n_{\text{m}}(T)$ was calculated from the $f_{\text{ice}}(T)$ data, and the results from the LOC-NIPI and μL-NIPI are shown in Fig. 7a. The temperature errors are the same as in Fig. 4 for the $f_{\text{ice}}(T)$ data, while the $n_{\text{m}}(T)$ errors were calculated from the uncertainties in droplet volume, weighing errors, and Poisson counting errors derived from Monte Carlo simulations.[70,152,153] The LOC-NIPI and μL-NIPI datasets are clearly complementary, demonstrating a narrow

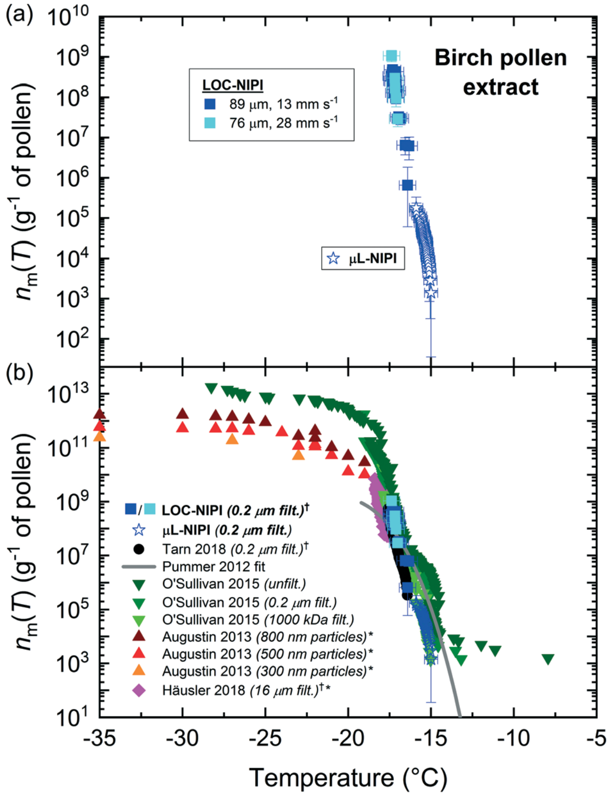

Fig. 7 Plots showing the active site density per mass of silver birch pollen extract (0.2 μm filtered). (a) Results obtained using the microfluidic LOC-NIPI platform (■) and the conventional μL-NIPI technique (☆), including all error bars. The average diameters and velocities of the droplets are provided in the legend. (b) Comparison of the LOC-NIPI and μL-NIPI results to literature data.[6,24,70,85,155,156] Only a handful of error bars are shown for clarity. Microfluidic data are indicated with †, and digitised data from the literature are indicated with *.

overall range of freezing temperatures and with the LOC-NIPI extending the $n_m(T)$ range of the μL-NIPI data.

The $n_m(T)$ data were also compared to data from the literature, as shown in Fig. 7b.[6,24,70,85,155,156] Microfluidic data are indicated with the symbol: †, while data that was digitised from plots in the research papers are indicated with the symbol: *. The LOC-NIPI data fits very well with the available literature data, including those obtained from our group in the past using the μL-NIPI[85] and a standard droplet assay using microfluidically-generated droplets (microfluidic pL-NIPI)[70] that utilised the same source of birch pollen (albeit a from a different batch).

The LOC-NIPI data also fell in a similar region to Häusler *et al.*,[24] who performed assays using an array of 40 μm diameter droplets on a microfabricated silicon wafer. The data was also relatively close to the Pummer *et al.*[155] parameterisation (provided by Murray *et al.*).[6] The size-segregated (300–800 nm) INP data from Augustin *et al.*[156] fell within different temperature and $n_m(T)$ ranges to the LOC-NIPI data, hence the two cannot be directly compared.

In summary, the LOC-NIPI results for birch pollen extract compared very well with the μL-NIPI data and to literature datasets, falling within the expected yet very narrow temperature range. The results also reiterated the interpretation of the Snomax® data that the flow rates and droplet velocities did not influence the freezing results within the flow rate range tested here, provided the temperature of the flowing oil in the chip is known. There is therefore the potential to further increase the flow rates to obtain higher droplet throughput, though this would need to be tested to determine the extent to which this could be achieved without incurring undesired effects. Far greater throughputs could be obtained by alterations to the chip design to limit the droplet cooling rates as they migrate over the cold plate and to allow greater control over the period of time spent over the coldest region of the cold plate, *e.g. via* the use of meandering serpentine channel features.

Aerosol samples from the Eastern Mediterranean

The results shown above demonstrate that the LOC-NIPI was capable of performing homogeneous nucleation and analysis of lab-prepared INP samples. In order to test its ability to analyse ambient INP samples, the LOC-NIPI was assessed by performing preliminary measurements during an atmospheric sampling campaign in the Eastern Mediterranean. A two week field campaign was undertaken in Rehovot, Israel, in October–November 2018 to measure the local atmospheric INP concentrations. The Eastern Mediterranean experiences dust storms[161–165] from the Saharan desert[162,164,166–168] and the Arabian desert,[162,164] air masses from Europe,[162,169,170] and sea-spray aerosol from the Mediterranean Sea,[161,170,171] making it a very interesting region in terms of aerosol and INP analysis.[172–175] The main findings of this field campaign will be discussed elsewhere, while the results here represented proof-of-concept trials of the LOC-NIPI in the field.

Aerosol samples were collected throughout the campaign, three of which were then analysed using the LOC-NIPI as an initial test of its viability in the field: (i) a filter-based sample collected for 3 h (3000 L of air, 44 ± 4 particles cm^{-3} of air as determined by an OPC), (ii) a filter-based sample collected for 24 h (24 000 L of air, 88 ± 75 particles cm^{-3} of air), and (iii) an impinger-based sample collected for 20 min (6000 L of air, 74 ± 4 particles cm^{-3} of air). Following the suspension of the collected aerosol particles in purified water, the suspensions were pumped into LOC-NIPI at a flow rate of 0.05 μL min^{-1} with an oil flow rate of 22 μL min^{-1} for analysis of the generated droplets (106 ± 10 μm diameter (CV = 8%); 11.9 ± 0.3 mm s^{-1} droplet velocities). Videos of the flowing droplets were recorded for 90 s at each cold plate set temperature, with 2 °C temperature increments applied to the cold plate set temperature. These parameters allowed the rapid analysis of the samples by scanning through the temperature range at a coarser temperature interval and for a shorter period of time than the previously described experiments, in order to determine whether it was possible to detect ambient INPs. It is worth noting that the number of droplets analysed helps to determines the effective temperature range covered; the more droplets analysed per temperature interval the more likely to detect rarer INPs that exhibit higher activities at higher temperatures.[104]

The fraction frozen, $f_{\mathrm{ice}}(T)$, results for the samples are shown in Fig. 8a alongside data from a blank of purified water (the same water used to prepare the aerosol samples). The first data point showing a signal for the blank (at $f_{\mathrm{ice}}(T) = 0.06$) was used to provide a baseline for the aerosol sample data at −35.3 °C, below which any sample data could be conservatively considered to be due to homogeneous freezing rather than the influence of INPs. Eqn (4) was used to calculate INP concentrations ($[\mathrm{INP}]_T$) from the three samples using the $f_{\mathrm{ice}}(T)$ data in Fig. 8a, with a V_{wash} of 4 mL, and using the V_{air} values associated with each individual sample (see Table S2 in the ESI‡). These $[\mathrm{INP}]_T$ results are shown in Fig. 8b. The dataset occupied a temperature range from −26.2 °C to −34.9 °C, and the INP concentrations covered around three orders of magnitude (~5–2100 INPs L^{-1}). The data points also show the number of frozen droplets and the total number of droplets analysed in each case in the format of $n_{\mathrm{ice}}(T)/n_{\mathrm{tot}}$, thus representing the $f_{\mathrm{ice}}(T)$ values. The number of droplets counted per video was lower than in the other analyses presented in the previous experiments due to time constraints during the campaign.

The three aerosol samples were also analysed *via* the μL-NIPI technique, using an array of 1 μL droplets, for comparison, and the results are shown in Fig. 8c alongside the LOC-NIPI data. The errors in $[\mathrm{INP}]_T$ were calculated based on uncertainties in droplet and washing volumes, and from Monte Carlo simulations that estimated the uncertainty due to a random distribution of active sites in the droplet in combination with Poisson uncertainties.[70,152,153] Due to the droplets in the μL-NIPI being much larger compared to the microfluidic droplets, there is a higher likelihood of rarer but more ice nucleation active particles (*i.e.* more efficient ice nucleators) being present. This has two major consequences: (i) the μL-NIPI has a baseline at higher temperatures due to the presence of contaminants and the droplet volume,[19] which can range from around −21 °C to −33 °C depending on the quality of the purified water, and (ii) the μL-NIPI results typically cover a higher temperature range than those of the LOC-NIPI data due to the sensitivity of the instrument to more active INPs that are in lower concentrations in that range.

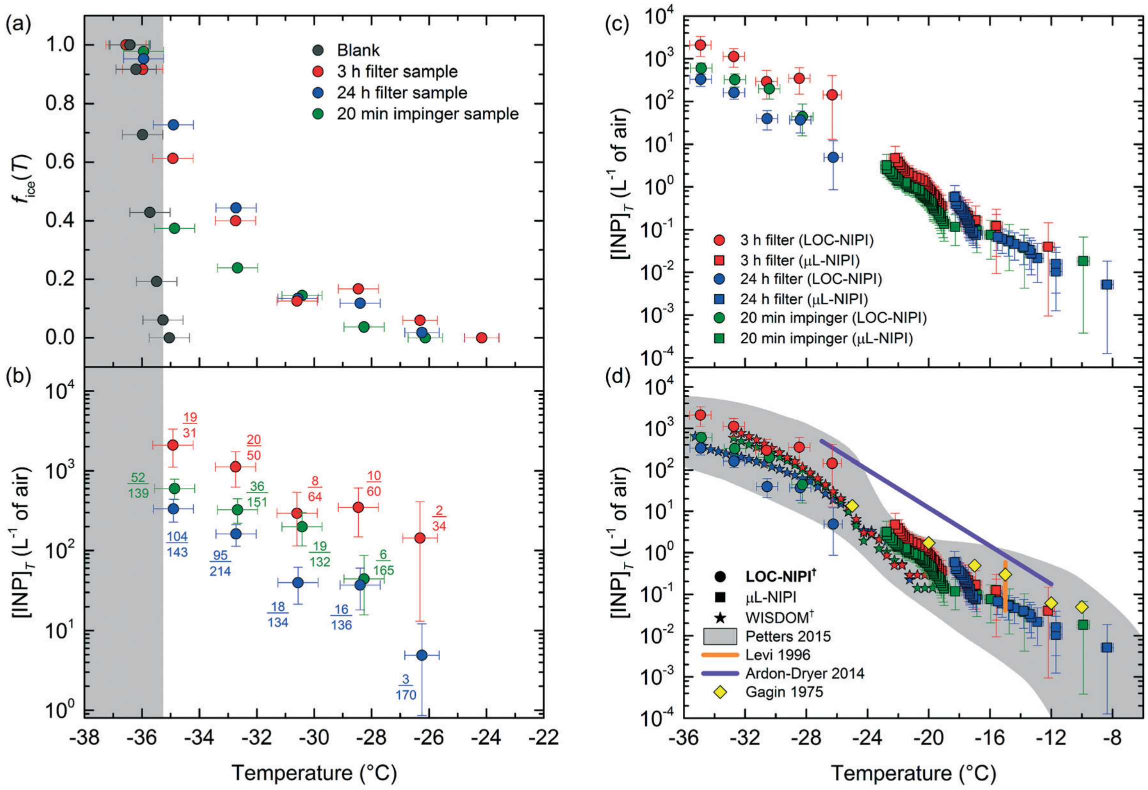

Fig. 8 Atmospheric INP measurements taken in the Eastern Mediterranean using the LOC-NIPI continuous flow platform. (a) $f_{\mathrm{ice}}(T)$ curves for: a blank consisting of purified water, a 3 h filter-based sample, a 24 h filter-based sample, and a 20 min impinger-based sample. (b) INP concentrations ($[\mathrm{INP}]_T$) for the aerosol samples analysed *via* the LOC-NIPI, based on the volume of air (in litres) collected for each sample (see Table S2 in the ESI‡). The fractions next to each data point represent the $n_{\mathrm{ice}}(T)/n_{\mathrm{tot}}$ (*i.e.* $f_{\mathrm{ice}}(T)$) for each experiment (see eqn (1)). (c) $[\mathrm{INP}]_T$ values for the samples analysed *via* both the LOC-NIPI (●) and the conventional μL-NIPI droplet assay (■), demonstrating their complementarity. (d) Comparison of the LOC-NIPI and μL-NIPI $[\mathrm{INP}]_T$ to literature data,[172–174,176] and to $[\mathrm{INP}]_T$ results obtained during the same campaign for aerosol collected *via* a MOUDI and analysed using the WISDOM microfluidic droplet array platform (★). The colours of the stars represent samples collected on the same days as those analysed by the LOC-NIPI and μL-NIPI, although sampling times and volumes varied between the instruments.

Whilst the results from the two techniques cannot be directly compared since they cover different ranges and populations of particles, given the limited number of droplets tested using the LOC-NIPI here, the data are complementary and consistent with each other, with the LOC-NIPI results extending the temperature and INP concentration ranges provided by the μL-NIPI technique. The 3 h filter and 20 min impinger samples in particular showed very similar trends between the two datasets, with the LOC-NIPI data appearing to act as a continuation of the μL-NIPI data as the temperature was lowered. The 24 h sample shows a somewhat similar trend, but this sample was exposed to both a short dust event and a long rain event that washed the aerosol out of the air, hence the huge variation in the ambient total particle concentrations (±86% from OPC readings) during that time period, and means that different particle populations may have been collected during the sampling time. The shorter collection times of the 3 h and 20 min samples were less susceptible to large changes in ambient particle populations and concentrations (±8% and ±5%, respectively, from OPC readings). We note that, since the samples were collected on different days, there is no expectation that the data from the different sampling times should be comparable for either analysis technique.

During the field campaign, aerosol samples were also collected using a MOUDI and analysed using the WISDOM microfluidic platform, in which a static array of 100 μm diameter droplets are frozen, to yield $[\mathrm{INP}]_T$ values as shown in Fig. 8d (as stars). The WISDOM results are shown for samples collected during the same days as those analysed by the LOC-NIPI and μL-NIPI, allowing for comparison with the caveat that variation is expected due to the different sampling times and strategies. Nonetheless, the results between the microfluidic platforms compared well despite operating in a different manner (*i.e.* continuous *vs.* static).

A handful of INP measurements have been taken in Israel previously, and these are also plotted in Fig. 8d for comparison. Gagin (1975) collected filter samples (100–300 L of air) at cloud base altitudes *via* aircraft and instrumentation on mountain terrain, before performing INP analysis using a static thermal diffusion chamber in the range of −10 to −25 °C.[172] Levi and Rosenfeld (1996) collected 3 h filter samples (100 L of air) at ground level (920 m a.s.l.) and analysed the INPs using a static thermal diffusion chamber at −15 °C.[173] Ardon-Dryer and Levin (2014) performed ground-based measurements (60 m a.s.l.) using filters (20 min sampling, 400 L of air) during dust events and "clean" days (*i.e.* without dust events), and during the Lag BaOmer bonfire event, with INP analysis achieved using the FRIDGE-TAU (Frankfurt Ice-nuclei Deposition freezing Experiment, the Tel Aviv University version) chamber that utilised an array of 1 μL droplets.[174] The datasets vary in their $[\mathrm{INP}]_T$ ranges and the measurement techniques largely explored higher temperature ranges than the LOC-NIPI and WISDOM instruments, but the lower temperature range of the Gagin 1975 data and the Ardon-Dryer and Levin 2014 data fell in a similar $[\mathrm{INP}]_T$ region to the microfluidic and μL-NIPI measurements.

Petters and Wright (2015) compiled INP concentrations determined from cloud water and precipitation samples around the globe between 1971–2014,[176] from which they generated an "envelope" of $[\mathrm{INP}]_T$ values to describe atmospheric INP concentrations (Fig. 8d). Both the LOC-NIPI and μL-NIPI data fit well within this envelope, indicating that the INP concentrations observed in the Eastern Mediterranean were within expected ranges, and offering further validation of the LOC-NIPI towards its use in the field. Future applications of the LOC-NIPI to field measurements would involve the use of smaller temperature increments, higher droplet throughput, and longer sampling times to achieve a larger number of droplet measurements that cover a wider temperature range with higher temperature resolution.

Outlook for the LOC-NIPI towards online INP monitoring

The LOC-NIPI has been demonstrated for the analysis of pure water and atmospheric INPs, including those from ambient samples. An in-depth discussion of the operational characteristic of the LOC-NIPI in different circumstances is provided in section 5 of the ESI,‡ including the effects of choosing different temperature increments and droplet numbers for different sets of experiments depending on the user's requirements. The results shown here suggest that the LOC-NIPI platform is applicable to INP analysis during field campaigns, and is suitable for use following both filter-based and impinger-based sampling. This provides a potential route for automated, online microfluidic droplet assay-based monitoring of INPs in the field that can cover a greater temperature range than CFDCs, albeit with a lower time resolution. However, a number of significant improvements over this prototype system will be required for this to become truly feasible, and these are discussed below:

(i) Automated video analysis will be very important development and is the more immediate concern; the initial results described here were obtained by manually counting droplets in each video. Whilst acceptable for these proof-of-concept tests and for short studies, it is a time-consuming method of analysis that is not amenable to continuous monitoring, and inhibits the potential throughput of the platform. Automated image analysis could be relatively easily implemented by having a program detect and track droplets as they flow through the main channel, and to determine whether they have frozen based on the distinctive colour change during a nucleation event, similar to analysis programs demonstrated for other droplet assay techniques.[21,64,66,71,73] Thereafter, it is conceivable that a program could also be implemented to sequentially step through a series of temperature setpoints, holding the stage at each setpoint for a given duration of time or number of droplets to be analysed before moving to the next setpoint, thus providing a greater degree of automation. This would benefit all types of analysis performed using the LOC-NIPI, whether for the study of lab-prepared samples or field samples.

(ii) The results shown above for the field tests in the Eastern Mediterranean covered a range of ≤26 °C. As stated earlier, the effective temperature range covered by the platform depends on the number of droplets analysed; more droplets means a greater likelihood of detecting the rarer but more active INPs, *i.e.* those that trigger ice nucleation at warmer temperatures.[104] The LOC-NIPI could, in principle, detect freezing events approaching 0 °C (*e.g.* the Snomax® results showed that activity could be detected up to around −4 °C), with the compromise being that large numbers of droplets would need to be tested in order to obtain results at these temperatures, particularly when INP concentrations are low. In future campaigns, in which the LOC-NIPI will be used as a dedicated field instrument rather than simply for testing as shown here, greater droplet numbers will be analysed, particularly at the warmer temperatures, to ensure that a wider temperature range can be accessed by enabling more of the rarer, more active INPs to enter the platform. This would be assisted by washing the collected aerosol samples into smaller volumes of water in order to obtain higher concentrations of INPs in the droplets. Further, while the total volume of aqueous suspension analysed here was on the order of a microlitre due to its proof-of-concept nature, the study of a greater number of droplets would also allow a larger volume of the collected sample, and therefore a greater proportion of the INP population, to be assessed.

(iii) The LOC-NIPI would need to be integrated with a sampling system for automated field analysis. Impinger-based sampling is more amenable to this than filter-based sampling since particles are collected directly into water. The microfluidic device could then sample from the impinger using either peristaltic pumps, or a push-pull syringe pump setup with mechanisms in place for preventing particle sedimentation,[177] for continuous dispensing. However, a mechanism would then also need to be implemented for replacing the water in the impinger for each sample in order to avoid cross-contamination of samples. The LOC-NIPI could then run alongside aerosol particle sizing instruments in order to estimate the particle numbers and surface areas in the collected aerosol samples, such that important INP parameters like $n_s(T)$ could be calculated alongside $[\mathrm{INP}]_T$. Microfluidic methods could also potentially be employed rather than conventional impingers for directly sampling aerosol into a chip,[178–180] such as a microfluidic microimpinger,[181,182] a condensational growth tube collector,[183] an aerodynamic lens connected to a microfluidic droplet system,[184] electrostatic sampling,[185] or an electrostatic precipitator combined with an electrowetting-on-dielectric (EWOD) concentrator.[186] However, due to the relative rarity of INPs in the atmosphere that can vary widely with location, higher flow rate sampling methods are likely required and so an impinger-based system, such as the Coriolis® Micro used in this study, may be the better option for future development of the platform.

Conclusions

We have developed a microfluidic platform, the LOC-NIPI, for the analysis of atmospheric ice-nucleating particles (INPs) *via* the freezing of droplets in continuous flow, and have performed validation studies and initial field tests during a sampling campaign. Water-in-oil droplets containing aqueous suspensions of INPs were generated and passed over a sub-zero temperature cold plate, whereupon droplet freezing events were recorded to provide information on the activity and concentration of INPs. The LOC-NIPI was tested using water, Snomax® and birch pollen extract, with hundreds of droplets analysed per temperature and several thousand per experiment. The results were reproducible and compared well to both conventional 1 μL droplet assays and to data available in the literature. It was also deployed during a campaign in the Eastern Mediterranean where analysis was performed on aerosol samples collected by both filter-based and impinger-based methods. The platform and the microfluidic device were designed to be easy to operate by non-microfluidicists, with the chip requiring only a simple PDMS fabrication process and the use of an insertable temperature probe for temperature measurements.

Performing immersion freezing analysis in continuous flow allows the user to define the number of droplets analysed per temperature and per sample in order to improve the statistics of the analysis, and enables the entire temperature range from 0 °C to homogeneous freezing (≲−35 °C) to be covered. Further development of the platform will involve automation of the video analysis and temperature sequences as a means to increasing its user-friendliness and automation. Integration with an aerosol sampling system will further enable continuous, autonomous monitoring of INPs in the field. While the initial focus of the LOC-NIPI has been related to ice nucleation in the atmosphere, the platform will also be applicable to areas outside of atmospheric science, for example in cryobiology where it could be used to test the ice-nucleating ability of biological species or in the development of cryoprotectants.

Conflicts of interest

There are no conflicts to declare.

Acknowledgements

The authors thank the European Research Council (ERC: 648661 MarineIce), the Natural Environment Research Council (NERC: NE/M010473/1), and the Weizmann–UK Making Connections Program for funding. B. V. W. thanks the Engineering and Physical Sciences Research Council (EPSRC: EP/R513258/1) for a studentship. B. J. M. and J.-u. S. contributed equally to the leadership of this work. Liam Hunter and Matthew Bourn are acknowledged for helpful discussions. Anthony Windross, Stephen Burgess, and Harri Wyn Williams are thanked for the fabrication of various components of the cold stage platform. Benjamin R. G.

Johnson is thanked for 3D printing of the prototype cold stage body and for performing the chromium evaporation process for coating the glass substrates of the microfluidic devices. Mark A. Holden and Alberto Sánchez-Marroquín are acknowledged for comments on the manuscript. Thomas Koop and Carsten Budke are thanked for their data from Budke and Koop (2015),[21] while Michael Polen and Ryan Sullivan are thanked for providing their data from Polen *et al.* (2016).[150]

Notes and references

1 U. Lohmann and J. Feichter, *Atmos. Chem. Phys.*, 2005, **5**, 715–737.

2 J. Haywood and O. Boucher, *Rev. Geophys.*, 2000, **38**, 513–543.

3 D. Lamb and J. Verlinde, *Physics and Chemistry of Clouds*, Cambridge University Press, Cambridge, 2011.

4 R. J. Herbert, B. J. Murray, S. J. Dobbie and T. Koop, *Geophys. Res. Lett.*, 2015, **42**, 1599–1605.

5 H. R. Pruppacher and J. D. Klett, *Microphysics of Clouds and Precipitation*, Kluwer Academic Publishers, Dordrecht, 1997.

6 B. J. Murray, D. O'Sullivan, J. D. Atkinson and M. E. Webb, *Chem. Soc. Rev.*, 2012, **41**, 6519–6554.

7 C. Hoose and O. Möhler, *Atmos. Chem. Phys.*, 2012, **12**, 9817–9854.

8 J. Vergara-Temprado, A. K. Miltenberger, K. Furtado, D. P. Grosvenor, B. J. Shipway, A. A. Hill, J. M. Wilkinson, P. R. Field, B. J. Murray and K. S. Carslaw, *Proc. Natl. Acad. Sci. U. S. A.*, 2018, **115**, 2687–2692.

9 C. Marcolli, *Atmos. Chem. Phys.*, 2014, **14**, 2071–2104.

10 G. Vali, P. J. DeMott, O. Möhler and T. F. Whale, *Atmos. Chem. Phys.*, 2015, **15**, 10263–10270.

11 D. Barahona, *Atmos. Chem. Phys.*, 2018, **18**, 17119–17141.

12 A. Wiacek, T. Peter and U. Lohmann, *Atmos. Chem. Phys.*, 2010, **10**, 8649–8667.

13 N. Hiranuma, S. Augustin-Bauditz, H. Bingemer, C. Budke, J. Curtius, A. Danielczok, K. Diehl, K. Dreischmeier, M. Ebert, F. Frank, N. Hoffmann, K. Kandler, A. Kiselev, T. Koop, T. Leisner, O. Möhler, B. Nillius, A. Peckhaus, D. Rose, S. Weinbruch, H. Wex, Y. Boose, P. J. DeMott, J. D. Hader, T. C. J. Hill, Z. A. Kanji, G. Kulkarni, E. J. T. Levin, C. S. McCluskey, M. Murakami, B. J. Murray, D. Niedermeier, M. D. Petters, D. O'Sullivan, A. Saito, G. P. Schill, T. Tajiri, M. A. Tolbert, A. Welti, T. F. Whale, T. P. Wright and K. Yamashita, *Atmos. Chem. Phys.*, 2015, **15**, 2489–2518.

14 H. Wex, S. Augustin-Bauditz, Y. Boose, C. Budke, J. Curtius, K. Diehl, A. Dreyer, F. Frank, S. Hartmann, N. Hiranuma, E. Jantsch, Z. A. Kanji, A. Kiselev, T. Koop, O. Möhler, D. Niedermeier, B. Nillius, M. Rösch, D. Rose, C. Schmidt, I. Steinke and F. Stratmann, *Atmos. Chem. Phys.*, 2015, **15**, 1463–1485.

15 P. J. DeMott, O. Möhler, D. J. Cziczo, N. Hiranuma, M. D. Petters, S. S. Petters, F. Belosi, H. G. Bingemer, S. D. Brooks, C. Budke, M. Burkert-Kohn, K. N. Collier, A. Danielczok, O. Eppers, L. Felgitsch, S. Garimella, H. Grothe, P. Herenz, T. C. J. Hill, K. Höhler, Z. A. Kanji, A. Kiselev, T. Koop, T. B. Kristensen, K. Krüger, G. Kulkarni, E. J. T. Levin, B. J. Murray, A. Nicosia, D. O'Sullivan, A. Peckhaus, M. J. Polen, H. C. Price, N. Reicher, D. A. Rothenberg, Y. Rudich, G. Santachiara, T. Schiebel, J. Schrod, T. M. Seifried, F. Stratmann, R. C. Sullivan, K. J. Suski, M. Szakáll, H. P. Taylor, R. Ullrich, J. Vergara-Temprado, R. Wagner, T. F. Whale, D. Weber, A. Welti, T. W. Wilson, M. J. Wolf and J. Zenker, *Atmos. Meas. Tech.*, 2018, **11**, 6231–6257.

16 P. J. DeMott, T. C. J. Hill, M. D. Petters, A. K. Bertram, Y. Tobo, R. H. Mason, K. J. Suski, C. S. McCluskey, E. J. T. Levin, G. P. Schill, Y. Boose, A. M. Rauker, A. J. Miller, J. Zaragoza, K. Rocci, N. E. Rothfuss, H. P. Taylor, J. D. Hader, C. Chou, J. A. Huffman, U. Pöschl, A. J. Prenni and S. M. Kreidenweis, *Atmos. Chem. Phys.*, 2017, **17**, 11227–11245.

17 N. Hiranuma, K. Adachi, D. M. Bell, F. Belosi, H. Beydoun, B. Bhaduri, H. Bingemer, C. Budke, H. C. Clemen, F. Conen, K. M. Cory, J. Curtius, P. J. DeMott, O. Eppers, S. Grawe, S. Hartmann, N. Hoffmann, K. Höhler, E. Jantsch, A. Kiselev, T. Koop, G. Kulkarni, A. Mayer, M. Murakami, B. J. Murray, A. Nicosia, M. D. Petters, M. Piazza, M. Polen, N. Reicher, Y. Rudich, A. Saito, G. Santachiara, T. Schiebel, G. P. Schill, J. Schneider, L. Segev, E. Stopelli, R. C. Sullivan, K. Suski, M. Szakáll, T. Tajiri, H. Taylor, Y. Tobo, R. Ullrich, D. Weber, H. Wex, T. F. Whale, C. L. Whiteside, K. Yamashita, A. Zelenyuk and O. Möhler, *Atmos. Chem. Phys.*, 2019, **19**, 4823–4849.

18 D. C. Rogers, *Atmos. Res.*, 1988, **22**, 149–181.

19 G. Vali, *J. Atmos. Sci.*, 1971, **28**, 402–409.

20 T. F. Whale, B. J. Murray, D. O'Sullivan, T. W. Wilson, N. S. Umo, K. J. Baustian, J. D. Atkinson, D. A. Workneh and G. J. Morris, *Atmos. Meas. Tech.*, 2015, **8**, 2437–2447.

21 C. Budke and T. Koop, *Atmos. Meas. Tech.*, 2015, **8**, 689–703.

22 Y. Tobo, *Sci. Rep.*, 2016, **6**, 32930.

23 A. D. Harrison, T. F. Whale, R. Rutledge, S. Lamb, M. D. Tarn, G. C. E. Porter, M. P. Adams, J. B. McQuaid, G. J. Morris and B. J. Murray, *Atmos. Meas. Tech.*, 2018, **11**, 5629–5641.

24 T. Häusler, L. Witek, L. Felgitsch, R. Hitzenberger and H. Grothe, *Atmosphere*, 2018, **9**, 140.

25 C. S. McCluskey, T. C. J. Hill, F. Malfatti, C. M. Sultana, C. Lee, M. V. Santander, C. M. Beall, K. A. Moore, G. C. Cornwell, D. B. Collins, K. A. Prather, T. Jayarathne, E. A. Stone, F. Azam, S. M. Kreidenweis and P. J. DeMott, *J. Atmos. Sci.*, 2016, **74**, 151–166.

26 K. J. Suski, T. C. J. Hill, E. J. T. Levin, A. Miller, P. J. DeMott and S. M. Kreidenweis, *Atmos. Chem. Phys.*, 2018, **18**, 13755–13771.

27 E. Garcia, T. C. J. Hill, A. J. Prenni, P. J. DeMott, G. D. Franc and S. M. Kreidenweis, *J. Geophys. Res.: Atmos.*, 2012, **117**, D18209.

28 P. J. DeMott, T. C. J. Hill, C. S. McCluskey, K. A. Prather, D. B. Collins, R. C. Sullivan, M. J. Ruppel, R. H. Mason, V. E. Irish, T. Lee, C. Y. Hwang, T. S. Rhee, J. R. Snider, G. R. McMeeking, S. Dhaniyala, E. R. Lewis, J. J. B.

Wentzell, J. Abbatt, C. Lee, C. M. Sultana, A. P. Ault, J. L. Axson, M. Diaz Martinez, I. Venero, G. Santos-Figueroa, M. D. Stokes, G. B. Deane, O. L. Mayol-Bracero, V. H. Grassian, T. H. Bertram, A. K. Bertram, B. F. Moffett and G. D. Franc, *Proc. Natl. Acad. Sci. U. S. A.*, 2016, **113**, 5797–5803.

29 E. J. T. Levin, P. J. DeMott, K. J. Suski, Y. Boose, T. C. J. Hill, C. S. McCluskey, G. P. Schill, K. Rocci, H. Al-Mashat, L. J. Kristensen, G. Cornwell, K. Prather, J. Tomlinson, F. Mei, J. Hubbe, M. Pekour, R. Sullivan, L. R. Leung and S. M. Kreidenweis, *J. Geophys. Res.: Atmos.*, 2019, **124**, 11530–11551.

30 C. S. McCluskey, J. Ovadnevaite, M. Rinaldi, J. Atkinson, F. Belosi, D. Ceburnis, S. Marullo, T. C. J. Hill, U. Lohmann, Z. A. Kanji, C. O'Dowd, S. M. Kreidenweis and P. J. DeMott, *J. Geophys. Res.: Atmos.*, 2018, **123**, 6196–6212.

31 P. J. DeMott, R. H. Mason, C. S. McCluskey, T. C. J. Hill, R. J. Perkins, Y. Desyaterik, A. K. Bertram, J. V. Trueblood, V. H. Grassian, Y. Qiu, V. Molinero, Y. Tobo, C. M. Sultana, C. Lee and K. A. Prather, *Environ. Sci.: Processes Impacts*, 2018, **20**, 1559–1569.

32 Y. Chen, S. M. Kreidenweis, L. M. McInnes, D. C. Rogers and P. J. DeMott, *Geophys. Res. Lett.*, 1998, **25**, 1391–1394.

33 D. C. Rogers, P. J. DeMott, S. M. Kreidenweis and Y. Chen, *J. Atmos. Ocean. Technol.*, 2001, **18**, 725–741.

34 C. Chou, O. Stetzer, E. Weingartner, Z. Jurányi, Z. A. Kanji and U. Lohmann, *Atmos. Chem. Phys.*, 2011, **11**, 4725–4738.

35 S. Garimella, T. B. Kristensen, K. Ignatius, A. Welti, J. Voigtländer, G. R. Kulkarni, F. Sagan, G. L. Kok, J. Dorsey, L. Nichman, D. A. Rothenberg, M. Rösch, A. C. R. Kirchgäßner, R. Ladkin, H. Wex, T. W. Wilson, L. A. Ladino, J. P. D. Abbatt, O. Stetzer, U. Lohmann, F. Stratmann and D. J. Cziczo, *Atmos. Meas. Tech.*, 2016, **9**, 2781–2795.

36 K. Bi, G. R. McMeeking, D. P. Ding, E. J. T. Levin, P. J. DeMott, D. L. Zhao, F. Wang, Q. Liu, P. Tian, X. C. Ma, Y. B. Chen, M. Y. Huang, H. L. Zhang, T. D. Gordon and P. Chen, *J. Geophys. Res.: Atmos.*, 2019, **124**, 8065–8075.

37 S. Garimella, D. A. Rothenberg, M. J. Wolf, R. O. David, Z. A. Kanji, C. Wang, M. Rösch and D. J. Cziczo, *Atmos. Chem. Phys.*, 2017, **17**, 10855–10864.

38 P. J. DeMott, A. J. Prenni, G. R. McMeeking, R. C. Sullivan, M. D. Petters, Y. Tobo, M. Niemand, O. Möhler, J. R. Snider, Z. Wang and S. M. Kreidenweis, *Atmos. Chem. Phys.*, 2015, **15**, 393–409.

39 H. C. Price, K. J. Baustian, J. B. McQuaid, A. Blyth, K. N. Bower, T. Choularton, R. J. Cotton, Z. Cui, P. R. Field, M. Gallagher, R. Hawker, A. Merrington, A. Miltenberger, R. R. Neely, S. T. Parker, P. D. Rosenberg, J. W. Taylor, J. Trembath, J. Vergara-Temprado, T. F. Whale, T. W. Wilson, G. Young and B. J. Murray, *J. Geophys. Res.: Atmos.*, 2018, **123**, 2175–2193.

40 C. S. McCluskey, T. C. J. Hill, R. S. Humphries, A. M. Rauker, S. Moreau, P. G. Strutton, S. D. Chambers, A. G. Williams, I. McRobert, J. Ward, M. D. Keywood, J. Harnwell, W. Ponsonby, Z. M. Loh, P. B. Krummel, A. Protat, S. M. Kreidenweis and P. J. DeMott, *Geophys. Res. Lett.*, 2018, **45**, 11989–911997.

41 A. Peckhaus, A. Kiselev, T. Hiron, M. Ebert and T. Leisner, *Atmos. Chem. Phys.*, 2016, **16**, 11477–11496.

42 A. Abdelmonem, E. H. G. Backus, N. Hoffmann, M. A. Sánchez, J. D. Cyran, A. Kiselev and M. Bonn, *Atmos. Chem. Phys.*, 2017, **17**, 7827–7837.

43 M. D. Tarn and N. Pamme, in *Elsevier Reference Module in Chemistry, Molecular Sciences and Chemical Engineering*, ed. J. Reedijk, Elsevier, Waltham, MA, 2013, DOI: 10.1016/B978-0-12-409547-2.05351-8.

44 G. M. Whitesides, *Nature*, 2006, **442**, 368–373.

45 E. K. Sackmann, A. L. Fulton and D. J. Beebe, *Nature*, 2014, **507**, 181–189.

46 S.-Y. Teh, R. Lin, L.-H. Hung and A. P. Lee, *Lab Chip*, 2008, **8**, 198–220.

47 A. Huebner, S. Sharma, M. Srisa-Art, F. Hollfelder, J. B. Edel and A. J. deMello, *Lab Chip*, 2008, **8**, 1244–1254.

48 P. Zhu and L. Wang, *Lab Chip*, 2017, **17**, 34–75.

49 W.-L. Chou, P.-Y. Lee, C.-L. Yang, W.-Y. Huang and Y.-S. Lin, *Micromachines*, 2015, **6**, 1249.

50 H. Shi, Y. Xiao, S. Ferguson, X. Huang, N. Wang and H. Hao, *Lab Chip*, 2017, **17**, 2167–2185.

51 Y. Ding, P. D. Howes and A. J. deMello, *Anal. Chem.*, 2020, **92**, 132–149.

52 A. Mousson, *Ann. Phys.*, 1858, **181**, 161–174.

53 A. Mousson, *Bibl. Univers. Geneve*, 1858, **3**, 296.

54 H. C. Sorby, *Philos. Mag.*, 1859, **18**, 105–108.

55 M. L. Dufour, *Philos. Mag.*, 1861, **21**, 543–544.

56 R. G. Dorsch and P. T. Hacker, *National Advisory Committee for Aeronautics, Technical Note 2142*, 1950.

57 G. Van der Mensbrugge, *Philos. Mag.*, 1876, **2**, 450–458.

58 G. Van der Mensbrugge, *Philos. Mag.*, 1877, **4**, 40–48.

59 S. C. Mossop, *Proc. Phys. Soc., B*, 1955, **68**, 193.

60 R. S. Chahal and R. D. Miller, *Br. J. Appl. Phys.*, 1965, **16**, 231.

61 B. Vonnegut, *J. Colloid Interface Sci.*, 1948, **3**, 563–569.

62 C. L. Hosler and C. R. Hosler, *Trans., Am. Geophys. Union*, 1955, **36**, 126–132.

63 J. F. Edd, K. J. Humphry, D. Irimia, D. A. Weitz and M. Toner, *Lab Chip*, 2009, **9**, 1859–1865.

64 C. A. Stan, G. F. Schneider, S. S. Shevkoplyas, M. Hashimoto, M. Ibanescu, B. J. Wiley and G. M. Whitesides, *Lab Chip*, 2009, **9**, 2293–2305.

65 C. A. Stan, S. K. Y. Tang, K. J. M. Bishop and G. M. Whitesides, *J. Phys. Chem. B*, 2011, **115**, 1089–1097.

66 B. Riechers, F. Wittbracht, A. Huetten and T. Koop, *Phys. Chem. Chem. Phys.*, 2013, **15**, 5873–5887.

67 L. Weng, S. N. Tessier, K. Smith, J. F. Edd, S. L. Stott and M. Toner, *Langmuir*, 2016, **32**, 9229–9236.

68 L. Weng, A. Swei and M. Toner, *Cryobiology*, 2018, **84**, 91–94.

69 A. E. Sgro, P. B. Allen and D. T. Chiu, *Anal. Chem.*, 2007, **79**, 4845–4851.

70 M. D. Tarn, S. N. F. Sikora, G. C. E. Porter, D. O'Sullivan, M. Adams, T. F. Whale, A. D. Harrison, J. Vergara-Temprado,

T. W. Wilson, J.-u. Shim and B. J. Murray, *Microfluid. Nanofluid.*, 2018, **22**, 52.

71 N. Reicher, L. Segev and Y. Rudich, *Atmos. Meas. Tech.*, 2018, **11**, 233–248.

72 A. E. Sgro and D. T. Chiu, *Lab Chip*, 2010, **10**, 1873–1877.

73 T. Brubaker, M. Polen, P. Cheng, V. Ekambaram, J. Somers, S. L. Anna and R. C. Sullivan, *Aerosol Sci. Technol.*, 2020, **54**, 79–93.

74 D. Atig, A. Touil, M. Ildefonso, L. Marlin, P. Bouriat and D. Broseta, *Chem. Eng. Sci.*, 2018, **192**, 1189–1197.

75 Y. Zhang and H.-R. Jiang, *Anal. Chim. Acta*, 2016, **914**, 7–16.

76 L.-J. Pan, J.-W. Tu, H.-T. Ma, Y.-J. Yang, Z.-Q. Tian, D.-W. Pang and Z.-L. Zhang, *Lab Chip*, 2018, **18**, 41–56.

77 M. Serra, D. Ferraro, I. Pereiro, J. L. Viovy and S. Descroix, *Lab Chip*, 2017, **17**, 3979–3999.

78 P. C. Gach, K. Iwai, P. W. Kim, N. J. Hillson and A. K. Singh, *Lab Chip*, 2017, **17**, 3388–3400.

79 M. Sesen, T. Alan and A. Neild, *Lab Chip*, 2017, **17**, 2372–2394.

80 T. S. Kaminski, O. Scheler and P. Garstecki, *Lab Chip*, 2016, **16**, 2168–2187.

81 M. T. Guo, A. Rotem, J. A. Heyman and D. A. Weitz, *Lab Chip*, 2012, **12**, 2146–2155.

82 K. A. Hagan, C. R. Reedy, J. M. Bienvenue, A. H. Dewald and J. P. Landers, *Analyst*, 2011, **136**, 1928–1937.

83 C. J. Easley, J. M. Karlinsey, J. M. Bienvenue, L. A. Legendre, M. G. Roper, S. H. Feldman, M. A. Hughes, E. L. Hewlett, T. J. Merkel, J. P. Ferrance and J. P. Landers, *Proc. Natl. Acad. Sci. U. S. A.*, 2006, **103**, 19272.

84 3M™ Novec™ 7500 Engineered Fluid - Product Information, 3M Company, accessed July 2020, http://multimedia.3m.com/mws/media/65496O/3mtm-novectm-7500-engineered-fluid.pdf.

85 D. O'Sullivan, B. J. Murray, J. F. Ross, T. F. Whale, H. C. Price, J. D. Atkinson, N. S. Umo and M. E. Webb, *Sci. Rep.*, 2015, **5**, 8082.

86 A. Iles, R. Fortt and A. J. de Mello, *Lab Chip*, 2005, **5**, 540–544.

87 S. L. Anna, N. Bontoux and H. A. Stone, *Appl. Phys. Lett.*, 2003, **82**, 364–366.

88 L. Mazutis, J. Gilbert, W. L. Ung, D. A. Weitz, A. D. Griffiths and J. A. Heyman, *Nat. Protoc.*, 2013, **8**, 870–891.

89 K. W. Oh, K. Lee, B. Ahn and E. P. Furlani, *Lab Chip*, 2012, **12**, 515–545.

90 C. S. Effenhauser, G. J. M. Bruin, A. Paulus and M. Ehrat, *Anal. Chem.*, 1997, **69**, 3451–3457.

91 D. C. Duffy, J. C. McDonald, O. J. A. Schueller and G. M. Whitesides, *Anal. Chem.*, 1998, **70**, 4974–4984.

92 J. C. McDonald, D. C. Duffy, J. R. Anderson, D. T. Chiu, H. Wu, O. J. A. Schueller and G. M. Whitesides, *Electrophoresis*, 2000, **21**, 27–40.

93 C. Holtze, A. C. Rowat, J. J. Agresti, J. B. Hutchison, F. E. Angile, C. H. J. Schmitz, S. Koster, H. Duan, K. J. Humphry, R. A. Scanga, J. S. Johnson, D. Pisignano and D. A. Weitz, *Lab Chip*, 2008, **8**, 1632–1639.

94 J.-u. Shim, L. F. Olguin, G. Whyte, D. Scott, A. Babtie, C. Abell, W. T. S. Huck and F. Hollfelder, *J. Am. Chem. Soc.*, 2009, **131**, 15251–15256.

95 F. Schuler, M. Trotter, M. Geltman, F. Schwemmer, S. Wadle, E. Dominguez-Garrido, M. Lopez, C. Cervera-Acedo, P. Santibanez, F. von Stetten, R. Zengerle and N. Paust, *Lab Chip*, 2016, **16**, 208–216.

96 L. Zhang, Q. Cai, R. S. Wiederkehr, M. Fauvart, P. Fiorini, B. Majeed, M. Tsukuda, T. Matsuno and T. Stakenborg, *Lab Chip*, 2016, **16**, 4012–4019.

97 M. Rhee, Y. K. Light, R. J. Meagher and A. K. Singh, *PLoS One*, 2016, **11**, e0153699.

98 D. Pekin, Y. Skhiri, J.-C. Baret, D. Le Corre, L. Mazutis, C. Ben Salem, F. Millot, A. El Harrak, J. B. Hutchison, J. W. Larson, D. R. Link, P. Laurent-Puig, A. D. Griffiths and V. Taly, *Lab Chip*, 2011, **11**, 2156–2166.

99 C. A. Stan, S. K. Y. Tang and G. M. Whitesides, *Anal. Chem.*, 2009, **81**, 2399–2402.

100 D. O'Sullivan, M. P. Adams, M. D. Tarn, A. D. Harrison, J. Vergara-Temprado, G. C. E. Porter, M. A. Holden, A. Sanchez-Marroquin, F. Carotenuto, T. F. Whale, J. B. McQuaid, R. Walshaw, D. H. P. Hedges, I. T. Burke, Z. Cui and B. J. Murray, *Sci. Rep.*, 2018, **8**, 13821.

101 J.-C. Soo, K. Monaghan, T. Lee, M. Kashon and M. Harper, *Aerosol Sci. Technol.*, 2016, **50**, 76–87.

102 W. G. Lindsley, in *NIOSH Manual of Analytical Methods (NMAM)*, Department of Health and Human Services, Centers for Disease Control and Prevention, National Institute for Occupational Safety and Health, 5th edn, 2016.

103 E. Stopelli, F. Conen, L. Zimmermann, C. Alewell and C. E. Morris, *Atmos. Meas. Tech.*, 2014, **7**, 129–134.

104 N. Reicher, C. Budke, L. Eickhoff, S. Raveh-Rubin, I. Kaplan-Ashiri, T. Koop and Y. Rudich, *Atmos. Chem. Phys.*, 2019, **19**, 11143–11158.

105 D. A. Knopf, P. A. Alpert, A. Zipori, N. Reicher and Y. Rudich, *npj Clim. Atmos. Sci.*, 2020, **3**, 2.

106 A. Zipori, N. Reicher, Y. Erel, D. Rosenfeld, A. Sandler, D. A. Knopf and Y. Rudich, *J. Geophys. Res.: Atmos.*, 2018, **123**, 12762–712777.

107 L. Eickhoff, K. Dreischmeier, A. Zipori, V. Sirotinskaya, C. Adar, N. Reicher, I. Braslavsky, Y. Rudich and T. Koop, *J. Phys. Chem. Lett.*, 2019, **10**, 966–972.

108 A. Bissoyi, N. Reicher, M. Chasnitsky, S. Arad, T. Koop, Y. Rudich and I. Braslavsky, *Biomolecules*, 2019, **9**, 532.

109 G. Vali, *J. Atmos. Sci.*, 1994, **51**, 1843–1856.

110 P. J. Connolly, O. Möhler, P. R. Field, H. Saathoff, R. Burgess, T. Choularton and M. Gallagher, *Atmos. Chem. Phys.*, 2009, **9**, 2805–2824.

111 D. Niedermeier, S. Hartmann, R. A. Shaw, D. Covert, T. F. Mentel, J. Schneider, L. Poulain, P. Reitz, C. Spindler, T. Clauss, A. Kiselev, E. Hallbauer, H. Wex, K. Mildenberger and F. Stratmann, *Atmos. Chem. Phys.*, 2010, **10**, 3601–3614.

112 M. Niemand, O. Möhler, B. Vogel, H. Vogel, C. Hoose, P. Connolly, H. Klein, H. Bingemer, P. DeMott, J. Skrotzki and T. Leisner, *J. Atmos. Sci.*, 2012, **69**, 3077–3092.

113 G. Vali, *Atmos. Chem. Phys.*, 2008, **8**, 5017–5031.

114 M. A. Holden, T. F. Whale, M. D. Tarn, D. O'Sullivan, R. D. Walshaw, B. J. Murray, F. C. Meldrum and H. K. Christenson, *Sci. Adv.*, 2019, **5**, eaav4316.

115 R. J. Herbert, B. J. Murray, T. F. Whale, S. J. Dobbie and J. D. Atkinson, *Atmos. Chem. Phys.*, 2014, **14**, 8501–8520.

116 D. Niedermeier, B. Ervens, T. Clauss, J. Voigtländer, H. Wex, S. Hartmann and F. Stratmann, *Geophys. Res. Lett.*, 2014, **41**, 736–741.

117 J. D. Atkinson, B. J. Murray and D. O'Sullivan, *J. Phys. Chem. A*, 2016, **120**, 6513–6520.

118 T. Koop and B. J. Murray, *J. Chem. Phys.*, 2016, **145**, 211915.

119 B. J. Murray, S. L. Broadley, T. W. Wilson, S. J. Bull, R. H. Wills, H. K. Christenson and E. J. Murray, *Phys. Chem. Chem. Phys.*, 2010, **12**, 10380–10387.

120 P. Stöckel, I. M. Weidinger, H. Baumgärtel and T. Leisner, *J. Phys. Chem. A*, 2005, **109**, 2540–2546.

121 P. Taborek, *Phys. Rev. B: Condens. Matter Mater. Phys.*, 1985, **32**, 5902–5906.

122 S. Benz, K. Megahed, O. Möhler, H. Saathoff, R. Wagner and U. Schurath, *J. Photochem. Photobiol., A*, 2005, **176**, 208–217.

123 B. Krämer, O. Hübner, H. Vortisch, L. Wöste, T. Leisner, M. Schwell, E. Rühl and H. Baumgärtel, *J. Chem. Phys.*, 1999, **111**, 6521–6527.

124 G. R. Wood and A. G. Walton, *J. Appl. Phys.*, 1970, **41**, 3027–3036.

125 L. Ladino, O. Stetzer, F. Lüönd, A. Welti and U. Lohmann, *J. Geophys. Res.: Atmos.*, 2011, **116**, D22202.

126 M. E. Earle, T. Kuhn, A. F. Khalizov and J. J. Sloan, *Atmos. Chem. Phys.*, 2010, **10**, 7945–7961.

127 B. H. Larson and B. D. Swanson, *J. Phys. Chem. A*, 2006, **110**, 1907–1916.

128 Snomax® International webpage, accessed July 2020, www.snomax.com.

129 A. S. Nezhad, *Lab Chip*, 2014, **14**, 2887–2904.

130 S. E. Lindow, D. C. Arny and C. D. Upper, *Plant Physiol.*, 1982, **70**, 1084–1089.

131 T. Šantl-Temkiv, M. Sahyoun, K. Finster, S. Hartmann, S. Augustin-Bauditz, F. Stratmann, H. Wex, T. Clauss, N. W. Nielsen, J. H. Sørensen, U. S. Korsholm, L. Y. Wick and U. G. Karlson, *Atmos. Environ.*, 2015, **109**, 105–117.

132 L. R. Maki, E. L. Galyan, M.-M. Chang-Chien and D. R. Caldwell, *Appl. Microbiol.*, 1974, **28**, 456–459.

133 G. Vali, M. Christensen, R. W. Fresh, E. L. Galyan, L. R. Maki and R. C. Schnell, *J. Atmos. Sci.*, 1976, **33**, 1565–1570.

134 O. Möhler, P. J. DeMott, G. Vali and Z. Levin, *Biogeosciences*, 2007, **4**, 1059–1071.

135 R. C. Schnell and G. Vali, *Nature*, 1972, **236**, 163–165.

136 R. C. Schnell and G. Vali, *Nature*, 1973, **246**, 212–213.

137 S. A. Yankofsky, Z. Levin, T. Bertold and N. Sandlerman, *J. Appl. Meteorol.*, 1981, **20**, 1013–1019.

138 R. L. Green and G. J. Warren, *Nature*, 1985, **317**, 645–648.

139 E. Garcia, T. C. J. Hill, A. J. Prenni, P. J. DeMott, G. D. Franc and S. M. Kreidenweis, *J. Geophys. Res.: Atmos.*, 2012, **117**, D18209.

140 T. C. J. Hill, B. F. Moffett, P. J. DeMott, D. G. Georgakopoulos, W. L. Stump and G. D. Franc, *Appl. Environ. Microbiol.*, 2014, **80**, 1256–1267.

141 C. E. Morris, F. Conen, J. Alex Huffman, V. Phillips, U. Pöschl and D. C. Sands, *Glob. Chang. Biol.*, 2014, **20**, 341–351.

142 C. E. Morris, C. L. Monteil and O. Berge, *Annu. Rev. Phytopathol.*, 2013, **51**, 85–104.

143 J. A. Huffman, A. J. Prenni, P. J. DeMott, C. Pöhlker, R. H. Mason, N. H. Robinson, J. Fröhlich-Nowoisky, Y. Tobo, V. R. Després, E. Garcia, D. J. Gochis, E. Harris, I. Müller-Germann, C. Ruzene, B. Schmer, B. Sinha, D. A. Day, M. O. Andreae, J. L. Jimenez, M. Gallagher, S. M. Kreidenweis, A. K. Bertram and U. Pöschl, *Atmos. Chem. Phys.*, 2013, **13**, 6151–6164.

144 V. R. Després, J. A. Huffman, S. M. Burrows, C. Hoose, A. S. Safatoc, G. Buryak, J. Fröhlich-Nowoisky, W. Elbert, M. O. Andrae, U. Pöschl and R. Jaenicke, *Tellus B*, 2012, **64**, 15598.

145 A. B. Michaud, J. E. Dore, D. Leslie, W. B. Lyons, D. C. Sands and J. C. Priscu, *J. Geophys. Res.: Atmos.*, 2014, **119**, 12186–112197.

146 B. C. Christner, R. Cai, C. E. Morris, K. S. McCarter, C. M. Foreman, M. L. Skidmore, S. N. Montross and D. C. Sands, *Proc. Natl. Acad. Sci. U. S. A.*, 2008, **105**, 18854–18859.

147 B. C. Christner, C. E. Morris, C. M. Foreman, R. Cai and D. C. Sands, *Science*, 2008, **319**, 1214.

148 M. Joly, E. Attard, M. Sancelme, L. Deguillaume, C. Guilbaud, C. E. Morris, P. Amato and A.-M. Delort, *Atmos. Environ.*, 2013, **70**, 392–400.

149 R. Du, P. Du, Z. Lu, W. Ren, Z. Liang, S. Qin, Z. Li, Y. Wang and P. Fu, *Sci. Rep.*, 2017, **7**, 39673.

150 M. Polen, E. Lawlis and R. C. Sullivan, *J. Geophys. Res.: Atmos.*, 2016, **121**, 11666–611678.

151 H. Beydoun, M. Polen and R. C. Sullivan, *Atmos. Chem. Phys.*, 2016, **16**, 13359–13378.

152 A. D. Harrison, T. F. Whale, M. A. Carpenter, M. A. Holden, L. Neve, D. O'Sullivan, J. Vergara Temprado and B. J. Murray, *Atmos. Chem. Phys.*, 2016, **16**, 10927–10940.

153 A. D. Harrison, K. Lever, A. Sanchez-Marroquin, M. A. Holden, T. F. Whale, M. D. Tarn, J. B. McQuaid and B. J. Murray, *Atmos. Chem. Phys.*, 2019, **19**, 11343–11361.

154 S. Pouleur, C. Richard, J.-G. Martin and H. Antoun, *Appl. Environ. Microbiol.*, 1992, **58**, 2960–2964.

155 B. G. Pummer, H. Bauer, J. Bernardi, S. Bleicher and H. Grothe, *Atmos. Chem. Phys.*, 2012, **12**, 2541–2550.

156 S. Augustin, H. Wex, D. Niedermeier, B. Pummer, H. Grothe, S. Hartmann, L. Tomsche, T. Clauss, J. Voigtländer, K. Ignatius and F. Stratmann, *Atmos. Chem. Phys.*, 2013, **13**, 10989–11003.

157 K. Dreischmeier, C. Budke, L. Wiehemeier, T. Kottke and T. Koop, *Sci. Rep.*, 2017, **7**, 41890.

158 A. L. Steiner, S. D. Brooks, C. Deng, D. C. O. Thornton, M. W. Pendleton and V. Bryant, *Geophys. Res. Lett.*, 2015, **42**, 3596–3602.

159 J. Sun and P. A. Ariya, *Atmos. Environ.*, 2006, **40**, 795–820.

160 J. D. Hader, T. P. Wright and M. D. Petters, *Atmos. Chem. Phys.*, 2014, **14**, 5433–5449.

161 Z. Levin, A. Teller, E. Ganor and Y. Yin, *J. Geophys. Res.: Atmos.*, 2005, **110**, D20202.

162 U. Dayan, *J. Clim. Appl. Meteorol.*, 1986, **25**, 591–595.

163 U. Dayan, J. Heffter, J. Miller and G. Gutman, *J. Appl. Meteorol.*, 1991, **30**, 1185–1199.

164 E. Ganor, *Atmos. Environ.*, 1994, **28**, 2867–2871.

165 Y. Mamane, E. Ganor and A. E. Donagi, *Water, Air, Soil Pollut.*, 1980, **14**, 29–43.

166 E. Ganor and Y. Mamane, *Atmos. Environ.*, 1982, **16**, 581–587.

167 D. H. Yaalon and E. Ganor, in *Saharan Dust: Mobilization, Transport, Deposition*, ed. C. Morales, John Wiley and Sons, New York, 1979, ch. 9, pp. 187–193.

168 E. Ganor, I. Osetinsky, A. Stupp and P. Alpert, *J. Geophys. Res.: Atmos.*, 2010, **115**, D07201.

169 A. Gagin, presented in part at the *Proceedings of the International Weather Modification Conference*, Canberra, Australia, 1971.

170 Z. Levin and J. D. Lindberg, *J. Geophys. Res.: Oceans*, 1979, **84**, 6941–6950.

171 Z. Levin, C. Price and E. Ganor, *Atmos. Environ., Part A*, 1990, **24**, 1143–1151.

172 A. Gagin, *J. Atmos. Sci.*, 1975, **32**, 1604–1614.

173 Y. Levi and D. Rosenfeld, *J. Appl. Meteorol.*, 1996, **35**, 1494–1501.

174 K. Ardon-Dryer and Z. Levin, *Atmos. Chem. Phys.*, 2014, **14**, 5217–5231.

175 Y. Boose, A. Welti, J. Atkinson, F. Ramelli, A. Danielczok, H. G. Bingemer, M. Plötze, B. Sierau, Z. A. Kanji and U. Lohmann, *Atmos. Chem. Phys.*, 2016, **16**, 15075–15095.

176 M. D. Petters and T. P. Wright, *Geophys. Res. Lett.*, 2015, **42**, 8758–8766.

177 S. I. R. Lane, J. Butement, J. Harrington, T. Underwood, J. Shrimpton and J. West, *Lab Chip*, 2019, **19**, 3771–3775.

178 A. R. Metcalf, S. Narayan and C. S. Dutcher, *Aerosol Sci. Technol.*, 2018, **52**, 310–329.

179 W. Jing and G. Sui, in *Recent Progress in Colloid and Surface Chemistry with Biological Applications*, American Chemical Society, 2015, ch. 13, vol. 1215, pp. 245–268.

180 X. Jiang, W. Jing, L. Zheng, W. Zhao and G. Sui, in *Proof and Concepts in Rapid Diagnostic Tests and Technologies*, ed. S. K. Saxena, InTech, Rijeka, 2016, ch. 5, DOI: 10.5772/63905.

181 I. Mirzaee, M. Song, M. Charmchi and H. Sun, *Lab Chip*, 2016, **16**, 2254–2264.

182 J. Choi, S. C. Hong, W. Kim and J. H. Jung, *ACS Sens.*, 2017, **2**, 513–521.

183 S. D. Noblitt, G. S. Lewis, Y. Liu, S. V. Hering, J. L. Collett and C. S. Henry, *Anal. Chem.*, 2009, **81**, 10029–10037.

184 B. Damit, *Aerosol Sci. Technol.*, 2017, **51**, 488–500.

185 Z. Ma, Y. Zheng, Y. Cheng, S. Xie, X. Ye and M. Yao, *J. Aerosol Sci.*, 2016, **95**, 84–94.

186 T. G. Foat, W. J. Sellors, M. D. Walker, P. A. Rachwal, J. W. Jones, D. D. Despeyroux, L. Coudron, I. Munro, D. K. McCluskey, C. K. L. Tan and M. C. Tracey, *J. Aerosol Sci.*, 2016, **95**, 43–53.

187 M. D. Tarn, S. N. F. Sikora, G. C. E. Porter, B. V. Wyld, M. Alayof, N. Reicher, A. D. Harrison, Y. Rudich, J.-u. Shim and B. J. Murray, Data for "On-chip analysis of atmospheric ice-nucleating particles in continuous flow", University of Leeds. [Dataset]. 2020, DOI: 10.5518/847.